SIMULATION STUDIES OF CONTROLLED LONGITUDINAL EMITTANCE BLOW-UP IN THE HL-LHC ERA

Author: Papadopoulou Paraskevi Anastasia

Supervisors:
Helga Timko [CERN]
Theodoros Gaitanos [Aristotle University of Thessaloniki]

CERN (European Organization for Nuclear Research)
ARISTOTLE UNIVERSITY OF THESSALONIKI

Switzerland, Geneva
2022

Ονειρεύομαι ανεύθυνα.
— Yoda Priest

To my parents…

Acknowledgments

I would like to express my sincere gratitude to my mentor and supervisor Dr. Helga Timko for her continuous guidance. Dr. Timko was present and helpful from day one during the whole time of research as well as writing this thesis. Her passion and her devotion to physics really motivated me during my studentship at CERN.
I would like to thank my supervisor, Prof. Theodoros Gaitanos for the assignation of this project.
Moreover, I would like to thank Dr. Theodoros Argyropoulos and Dr. Kostantinos Iliakis for their help.
Last but not least a big acknowledgement to my friends and colleagues Birk Karlsen-Baeck and Evin Vinten for their constant support and help.

Abstract

During the acceleration ramp of the LHC, single bunches would lose Landau damping longitudinally if their bunch emittance was preserved. Thus the LHC, by design, indispensably requires a controlled longitudinal emittance blow-up during the ramp to counteract loss of Landau damping. Controlled emittance blow-up has been operationally used since the start-up of the machine for nominal bunch intensities. The future High-Luminosity LHC project aims at doubling this intensity, and per se, it is not clear whether the presently operational method for the blow-up will still work at those intensities. In the past, simulation studies were conducted for nominal intensities and neglecting collective effects. In this thesis, we first review the threshold of loss of Landau damping in simulations and then we study blow-up for present and future beam intensities with collective effects. This is a computationally challenging task, even for single bunches, as it requires simulating the whole acceleration ramp of LHC, which is fourteen million turns long.

Περίληψη

Κατά την διαδικασία επιτάχυνσης στον μεγάλο επιταχυντή αδρονίων για μια διαμήκη δέσμη έχει παρατηρηθεί το φαινόμενο απόσβεσης $Landau$ αν η ένταση της δέσμης διατηρηθεί σταθερή. Ο συγκεκριμένος επιταχυντής απαιτεί ελεγχόμενη αύξηση της εκπεμπτικότητας ώστε να αντισταθμίσει το προαναφερθέν φαινόμενο. Στο παρελθόν είχαν γίνει αντίστοιχες μελέτες αλλά πάντα χωρίς τις επιδράσεις της έντασης του ρεύματος. Σε αυτή την πτυχιακή αρχικά μελετήσαμε το φαινόμενο απόσβεσης $Landau$ και έπειτα αναλύσαμε το φαινόμενο της ελεγχόμενης αύξησης της εκπεμπτικότητας λαμβάνοντας υπόψιν μας τις επιδράσεις της έντασης για τις παρούσες εντάσεις ρεύματος καθώς και τις μελλοντικές. Το πιο δύσκολο μέρος αυτής της μελέτης ήταν οι προσομοιώσεις της επιταχυνόμενης διάταξης του *LHC* για τα συγκεκριμένα μοντέλα καθώς ήταν αρκετά χρονοβόρα καθώς η διάταξη αποτελείται απο δεκατέσσερα εκατομμύριες στροφές.

Contents

List of Figures

1 Introduction

1.1 The CERN accelerator complex

CERN, the European Organization for Nuclear Research, is one of the world's largest laboratories for high-energy particle physics. It hosts a complex of machines that accelerates protons or ions close to the speed of light and delivers them to various experiments such as fixed-target experiments or the detectors of the Large Hadron Collider (LHC) [1]. Specifically, the acceleration chain for protons is the following: firstly particles start from the linear accelerator LINAC4, where they are accelerated to 160 MeV. Then, the particles pass to the Proton Synchrotron Booster (PSB), where their kinetic energies are increased to 2 GeV. Next in the sequence is the Proton Synchrotron (PS), which accelerates particles up to 25 GeV, before the injection into the Super Proton Synchrotron (SPS), which operates at up to 450 GeV. Finally, the particles are transferred to the LHC. In the LHC, the highest energy that a particle could be accelerated to was 6.5 TeV until 2018, while from 2022 onwards it is 6.8 TeV. The CERN accelerator complex is depicted in Fig. 1.1.

There are two kinds of accelerators: circular and linear; both have their benefits as well as their drawbacks. To be more specific, linear accelerators mainly need accelerating cavities, but each particle can be accelerated by a given cavity only once. The maximum energy achievable in a linear accelerator scales therefore with its length. On the other hand, circular accelerators require less accelerating cavities as they can accelerate the particles over and over again; however, to bend the particles, circular machines require many magnets. The maximum energy achievable in a circular accelerator is limited by synchrotron radiation and depends therefore on the radius of particle motion. Whether linear or circular accelerator, to achieve large energies, kilometer long machines are required.

1.2 The Large Hadron Collider

The world's biggest and highest-energy collider since 2008 has been the LHC [2]. Inside the LHC, two high-energy particle beams are circulating, each traveling in separate beam pipes

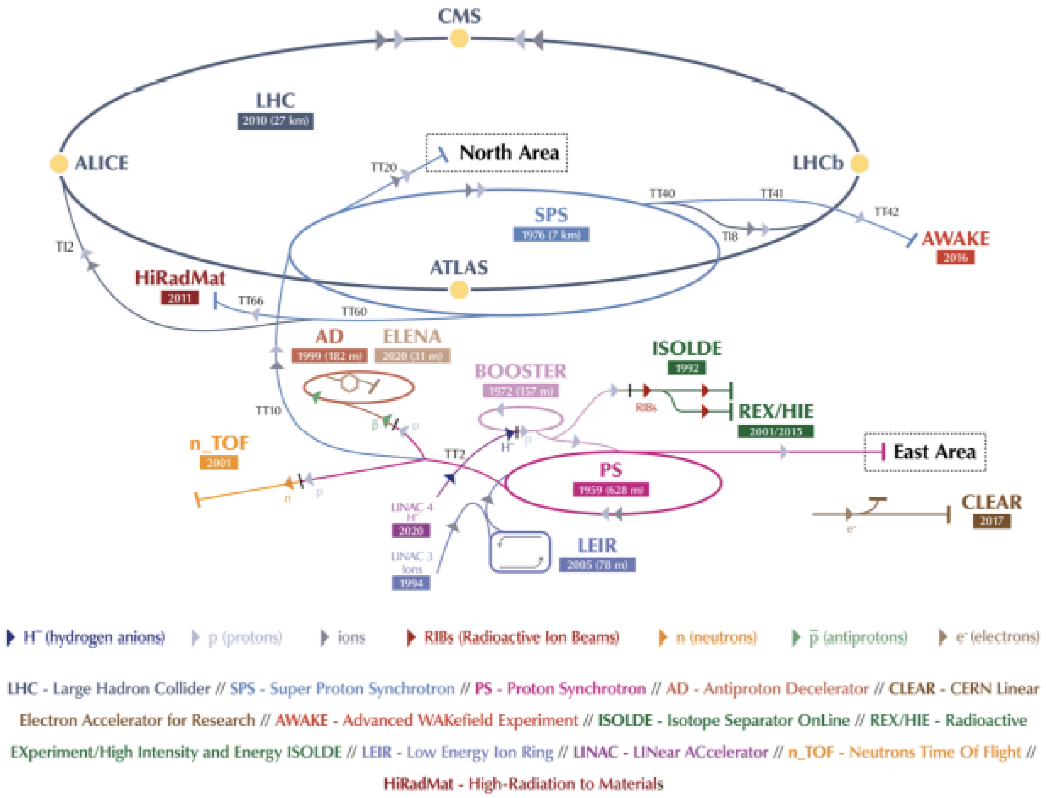

Figure 1.1: The CERN accelerator complex [1]

and in opposite directions. Its circumference is 27 km, and its main machine components are (i) superconducting magnets, whose magnetic field bends the beam so they can travel around the circular path of LHC, and (ii) superconducting, radio-frequency (RF) cavities, whose electric field accelerates the beam. The beams can be collided in four locations around the LHC. At these four locations, the main LHC detectors are placed: ALICE (A Large Ion Collider), ATLAS (A Toroidal LHC Apparatus), CMS (Compact Muon Solenoid) and LHCb (LHC-beauty). The detectors can be seen in Fig. 1.2.

The aforementioned magnets are placed inside a cryostat of superfluid Helium and work at a temperature of 1.9 K while the accelerating cavities work at 4.5 K [3]. The superconducting magnets were chosen for their compact size; normal-conducting magnets with 8.9 T wouldn't fit into the tunnel. Superconducting cavities were chosen for their small energy loss.

In this thesis we are focusing on charged particles that are moving in synchrotron. A synchrotron is a circular accelerator that synchronizes the frequency of the accelerating cavities with the bending field in the magnets.

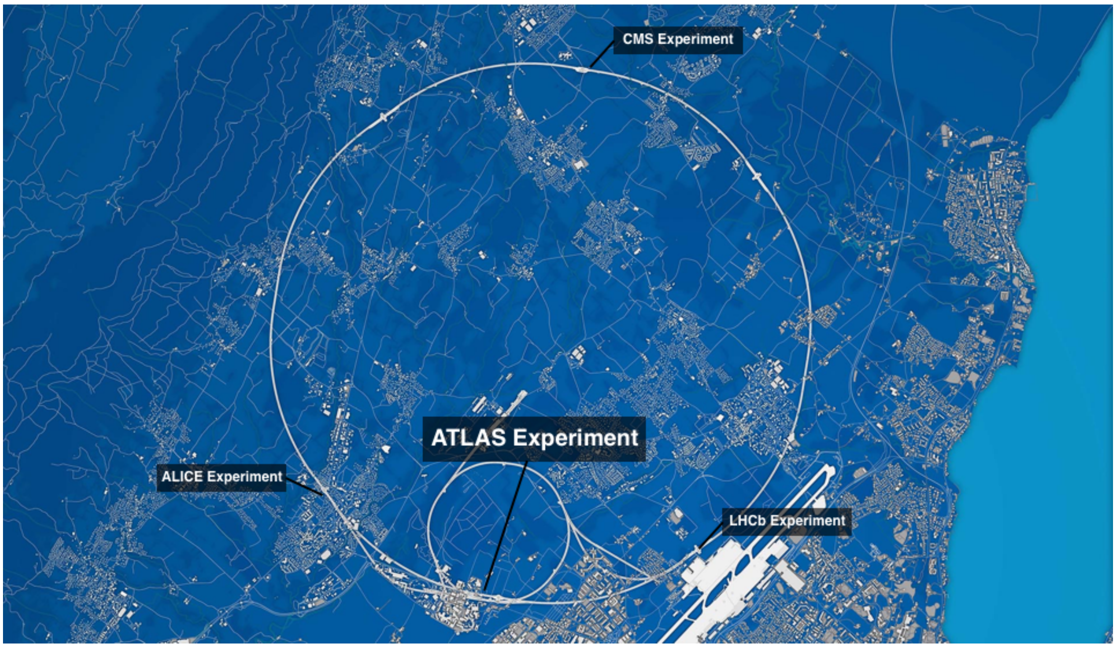

Figure 1.2: The location of the LHC detectors along the ring [1]

1.3 Accelerator physics and longitudinal beam dynamics

Accelerator physics is a branch of physics that studies the design, building, and operation of particle accelerators. Beam dynamics, a branch of accelerator physics, studies the motion of beam particles in an accelerator. The beam is usually packed into a dense volume around the minima of the potential well created by the electromagnetic fields in an accelerator; this dense collection of particles is called a "bunch". The word "beam" usually refers to the collection of all bunches and particles in a ring.

Beam dynamics can be further divided into describing longitudinal and transverse motion; longitudinal motion refers to the motion along the ring, while transverse motion happens in the cross-section of the accelerator. In this thesis, we will focus on longitudinal beam dynamics. A synchrotron consists of many elements that create or induce electromagnetic fields perturbing the motion of the charged particles travelling within it. The main potential well seen by the beam is created by the RF cavities, but it is perturbed by other induced fields that can lead to beam instabilities and losses. In general, the aim of beam dynamics is to study how to keep the beams in the synchrotrons stable and bunched.

1.4 Motivation for this thesis

As per design in the LHC Design Report [3], during the acceleration ramp in the LHC, loss of Landau damping (see Chapter 3) followed by beam instability and an uncontrolled emittance blow-up would occur, if the longitudinal emittance was to be kept constant. For this reason, controlled emittance blow-up was foreseen and has been used operationally since the beginning.

Measurement studies from the past have shown that depending on the speed of the ramp, the target bunch length, or the intensity of the beam, the controlled blow-up does not always regulate the emittance properly [4]. In the past, also simulation studies have been performed to optimize the blow-up for nominal beam intensities, but always neglecting collective effects.

1.5 Thesis outline

This bachelor thesis presents studies of the controlled blow-up emittance in the LHC, based on realistic conditions, by using a realistic impedance model and the nominal ramp of LHC. The studies are restricted to single proton bunches.

In the Chapter 2, an introduction to single-particle longitudinal beam dynamics is given. The parameters of LHC are detailed, as well as RF and beam parameters. An introduction to the low-level RF loops in the LHC is given, too.

In Chapter 3, loss of Landau damping during the ramp is studied in simulations with single bunches of different intensities and initial bunch lengths.

Chapter 4 describes the operational method used for controlled emittance blow-up RF phase noise generation used also in simulations.

The results of the simulations with controlled emittance blow-up are presented in Chapter 5.

2 Background

In this Chapter, the relevant background to this thesis concerning particle accelerators is given. We introduce the basic equations of motion for single-particle motion and their implementation in the BLonD simulation suite that has been used for the studies presented. Finally, beam control loops used in the LHC RF system are introduced.

2.1 Synchrotrons

2.1.1 Synchrotron radiation

Particle mass plays a dominant role in acceleration. Specifically, electrons reach a velocity v close to the speed of light c at relatively low energy E (order of 10 MeV), while heavier particles reach the same velocity only at much higher energies (see Fig. 2.1). For this plot we used the following set of equations:

$$p = mv = \frac{E}{c^2}\beta c = \beta\frac{E}{c} = \beta\gamma m_0 c\,, \tag{2.1}$$

where p is the particle momentum, $\beta = v/c$, m_0 is the rest mass of the particle, and E is the total energy for a particle, given by:

$$E = \gamma m_0 c^2\,. \tag{2.2}$$

The Lorentz factor γ is given by:

$$\gamma = \frac{E}{E_0} = \frac{m}{m_0} = \frac{1}{\sqrt{1-\beta^2}}\,. \tag{2.3}$$

One important reason for using protons in the LHC is that the maximum energy achievable in circular machines is limited due to synchrotron radiation. Every charged particle performing circular motion emits radiation; this results in energy loss and is thus slowing down the particle.

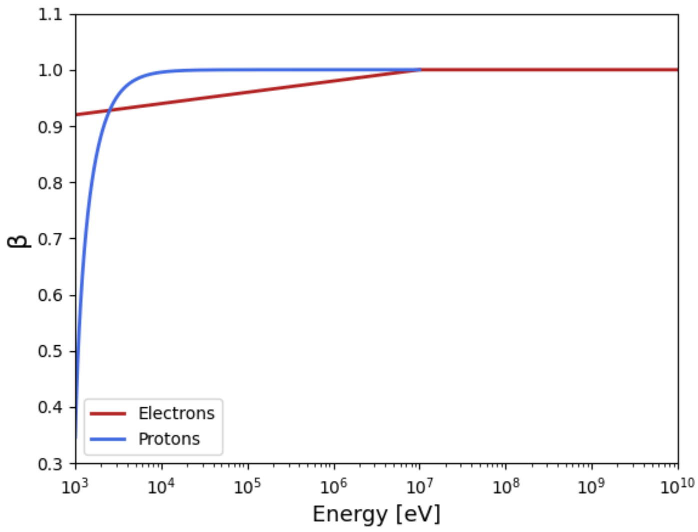

Figure 2.1: Relativistic β as a function of total energy; a comparison of electrons with protons

Table 2.1: Masses of particles

Proton	Electron
0.511 Mev	938 Mev

The heavier the particle, the higher the total energy that can be reached in a machine with a given ratio. The power radiated by a relativistic particle with energy E is [5]:

$$P_\gamma = \frac{cC_\gamma}{2\pi} \frac{E^4}{R\rho}, \tag{2.4}$$

where R is the average radius of the machine, ρ is the bending radius of the magnets, and $C_\gamma = 8.85 \times 10^{-5}$ [m/GeV^3].

The total energy radiated in one revolution is:

$$U_0 = \frac{C_\gamma E^4}{2\pi} \oint \frac{ds}{\rho^2}. \tag{2.5}$$

As we can see, the synchrotron radiation depends on the bending radius and particle energy.

The Large Electron Positron collider (LEP) collided electrons with positrons, from 1989 until 2000, in the same tunnel that hosts today the LHC. In 2001, it was dismantled in order to make way for LHC. In LEP, electrons at 100 GeV would radiate 2.9 GeV/turn, i.e. almost 3% of its total energy. On the other hand, protons in the LHC lose only 7 keV/turn at 7 TeV [3].

2.1.2 Lorentz force

In a synchrotron, a relativistic charged particle is trapped and accelerated by electromagnetic fields. To be more specific, the force F exerted on a particle with charge q traveling at a velocity $\vec{v}$ in the presence of an electric field $\mathscr{E}$ and a magnetic field $\mathscr{B}$ is described by the relativistic Lorentz force:

$$F = \frac{d\vec{p}}{dt} = q(\mathscr{E} + \vec{v} \times \mathscr{B})\,. \tag{2.6}$$

According to this equation, only the electric field can accelerate the particles while the magnetic field can change the direction of the particle's velocity. This is why cavities accelerate and magnets bend the beam particles.

Hence, it is necessary to have an electric field component along the longitudinal direction z to accelerate the particles:

$$\frac{dE}{dz} = v\frac{dp}{dz} = \frac{dp}{dt} = q\mathscr{E}_z. \tag{2.7}$$

2.2 Longitudinal beam dynamics

2.2.1 The synchronous particle

In a synchrotron, the particles are accelerated by the RF electric field in the accelerating structure. The voltage provided by the cavity can be written in the form of [5]:

$$V \sin\phi(t) = V \sin(\phi_s + \omega_{\mathrm{rf}} t)\,, \tag{2.8}$$

where V is the RF voltage amplitude, $\phi(t)$ is the RF phase that is being picked up by a particle traversing the cavity at time t, and ω_{rf} is the RF angular frequency. The phase ϕ_s is the RF phase of the so-called "synchronous particle" that traverses the cavity at multiples of the revolution period T_0. For the synchronous particle to come back to the cavity with ϕ_s again in the next turn, it has to carry the synchronous momentum p_s that corresponds to the magnetic strength at that moment along the ring.

Thus, the synchronous particle follows the exact or "designed" motion in the synchrotron. The synchrotron, on the other hand, synchronises the RF frequency in the cavities with the field strength of the magnets that bends the particles and determines how long a revolution or turn in the machine will take. This synchronisation implies that the RF frequency must be an integer multiple of the revolution frequency:

$$\omega_{\mathrm{rf}} = h\omega_0\,, \tag{2.9}$$

where h is the harmonic number and $\omega_0 = 2\pi/T_0$.

In longitudinal beam dynamics, it is a natural choice to use time and energy or momentum as the phase-space coordinates, and to describe the motion of all other particles w.r.t. the synchronous particle, using the following variables:

$$\begin{aligned} \Delta E &= E - E_s\,, \\ \Delta p &= p - p_s\,, \\ \Delta t &= t - t_s\,, \end{aligned} \tag{2.10}$$

where E_s and t_s are the energy and time coordinates of the synchronous particle, respectively. Due to its different energy and arrival time to the cavity, a non-synchronous particle will also experience a revolution frequency ω that slightly deviates from the machine's revolution frequency; its relative frequency can be defined therefore as:

$$\Delta\omega = \omega - \omega_0.$$

During the acceleration of a particle, the momentum starts to increase and so does the revolution frequency; this also affects the RF frequency. In general, during acceleration, a particle that has been synchronous from one turn to another, will not necessarily be synchronous in the subsequent turn. In other words, which particle is "synchronous" will change over time; it is an abstract particle and not a real particle whose motion can be followed.

2.2.2 Energy gain

To describe the energy gain of a particle when it passes through the RF cavity, we start from the expression of the electric field in the cavity based on Eqs. 2.8 and 2.9:

$$\mathscr{E} = \mathscr{E}_{\mathrm{rf}} \sin(h\omega_0 t + \phi_s)\,. \tag{2.11}$$

The revolution angular frequency ω_0 can also be expressed as:

$$\omega_0 = \frac{\beta_s c}{R_s}\,, \tag{2.12}$$

where β_s and R_s are the relativistic beta factor and the average radius or so-called "orbit" corresponding to the synchronous particle.

For an accelerating gap length g in the RF cavity, the passage of the synchronous particle will take the time $(-g/2\beta_s c, g/2\beta_s c)$ and its energy gain will be:

$$\Delta E = q\mathscr{E}_{\mathrm{rf}}\beta_s c \int_{-g/2\beta_s c}^{g/2\beta_s c} \sin(h\omega_0 t + \phi_s)\,dt \equiv q\mathscr{E}_{\mathrm{rf}} g T \sin\phi_s\,, \tag{2.13}$$

where T defines the transit-time factor

$$T = \frac{\sin(hg/2R_0)}{(hg/2R_0)}\,. \tag{2.14}$$

2.2.3 Equations of motion

Particle motion in a synchrotron is usually described on a turn-by-turn basis, as all changes in phase-space coordinates are slow compared to the revolution period. A key concept to derive the single-particle equations of motion in a synchrotron is the "slippage factor" η. The slippage factor is a property of the ring, describing the frequency slippage that an off-momentum particle experiences. It is defined through the relative frequency offset of a particle as follows:

$$\frac{\Delta\omega}{\omega_0} = \frac{\omega-\omega_0}{\omega_0} \equiv -\eta(\delta)\delta = -(\eta_0+\eta_1\delta+\eta_2^2\delta^2+...)\delta\,. \tag{2.15}$$

In the above expression, we have introduced also the relative momentum offset defined as

$$\delta \equiv \frac{\Delta p}{p_s} = \frac{\Delta E}{\beta_s^2 E_s}\,. \tag{2.16}$$

Using the concept of the slippage factor, the equations of motion can be derived to be [5]:

$$\frac{d}{dt}\left(\frac{\Delta E}{\omega_0}\right) = \frac{1}{2\pi}qV_0\left[\sin\phi-\sin\phi_s\right] \tag{2.17}$$

and

$$\frac{d\phi}{dt} = \frac{h\omega_0^2\eta}{\beta_s^2 E_s}\frac{\Delta E}{\omega_0}\,. \tag{2.18}$$

Equation 2.17 is referred to as the "kick" equation as it describes the energy kick given to the particle when it traverses the cavity. Equation 2.18 is known as the "drift" equation and describes the particle motion or slippage through the magnetic part of the machine.

Altogether, the Hamiltonian for the single-particle motion in a single RF system reads as follows:

$$H = \frac{1}{2}\frac{h\eta\omega_0^2}{\beta_s^2 E_s}\left(\frac{\Delta E}{\omega_0}\right)^2 + \frac{qV}{2\pi}\left[\cos\phi-\cos\phi_s+(\phi-\phi_s)\sin\phi_s\right]\,. \tag{2.19}$$

2.2.4 Small-amplitude oscillations

For particles whose coordinates are close to the synchronous particle, i.e. $\phi \approx \phi_s + \Delta\phi$, where $\Delta\phi \ll \pi$, the Hamiltonian in Eq. 2.19 reduces to

$$H = \frac{1}{2}\frac{h\eta_0\omega_0^2}{\beta_s^2 E_s}\left(\frac{\Delta E}{\omega_0}\right)^2 - \frac{qV\cos\phi_s}{2\pi}\left(\Delta\phi\right)^2 . \tag{2.20}$$

This is the Hamiltonian of a harmonic oscillator, with the frequency of oscillation being the central synchrotron frequency:

$$\omega_{s,0} = \omega_0\sqrt{\frac{hqV|\eta_0\cos\phi_s|}{2\pi\beta_s^2 E_s}} , \tag{2.21}$$

where, in order to obtain a restoring force, the expression $\eta_0\cos\phi_s < 0$. Under this condition, the motion is oscillatory, and beam particles organise into the dense structure that we call bunch.

2.2.5 Separatrix and RF bucket

The separatrix is the last closed orbit that is solution to the synchrotron Hamiltonian and is given by the equation:

$$\Delta E_{\text{sep}}(\phi) = \pm\sqrt{\frac{2\beta_s^2 E_s qV}{2\pi h\eta_0}\left(\cos(\pi-\phi_s) - \cos\phi + (\pi-\phi_s-\phi)\sin\phi_s\right)} , \tag{2.22}$$

assuming a single RF system and no collective effects. In accelerator physics, an “RF bucket” is one part of the separatrix in which a single bunch can be captured, see Fig. 2.2 (a figure after [6]).

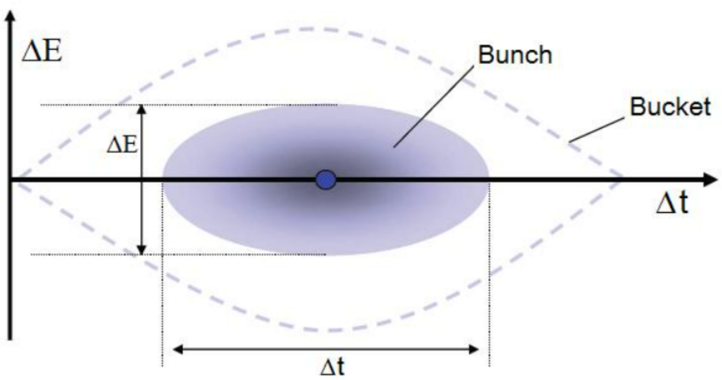

Figure 2.2: Sketch of an RF bucket (dashed line) and bunch distribution (shaded area) in $(\Delta t, \Delta E)$ phase space. The blue dot marks the synchronous particle.

For a non-accelerating bucket, the length of the bucket is the rf period T_{rf}, and the height of the bucket can be obtained from the maximum value of separatrix:

$$\Delta E_B = \frac{4\beta_s^2 E_s q V}{2\pi h \eta_0}. \tag{2.23}$$

In addition, the bucket area can be calculated by integrating Eq. 2.22:

$$A_B = \oint \Delta E_b(\phi) d\phi, \tag{2.24}$$

which for a non-accelerating bucket reduces to

$$A_B = 16\sqrt{\frac{qV}{2\pi\beta_s^2 E_s h|\eta|}}. \tag{2.25}$$

The emittance of a single particle is similarly defined by its contour in phase space:

$$\epsilon = \frac{4E\omega_{s,0}\beta^2}{\omega_{\text{rf}}^2\eta_0}\int_0^{\phi_b}\sqrt{2(\cos\phi - \cos\phi_b)}d\phi, \tag{2.26}$$

where ϕ_b is the maximum phase of the bunch.

2.2.6 Collective effects

In the above, we have seen how single particles move in the potential well created by the RF voltage. On the other hand, the circulating particles have an electric charge and a synchrotron is built of many components that can interact electromagnetically with these particles. The total machine impedance is typically described with a frequency-dependent impedance $Z(\omega)$, or its Fourier image, the so-called wakefield

$$W(t) = \frac{1}{2\pi}\int_{-\infty}^{\infty} d\omega Z(\omega) e^{i\omega t}. \tag{2.27}$$

In this context, the beam that consists of many charged particles can be describe with the function $\lambda(t)$, which is the beam profile or line density along the t-axis. The interaction of this beam with the impedance will induce a voltage that can be calculated in time domain as

$$V_{\text{ind,beam}}(\Delta t) = q\int_{-\infty}^{\infty} d\tau \lambda(\tau) W(\Delta t - \tau), \tag{2.28}$$

or equivalently, in frequency domain as

$$V_{\text{ind,beam}}(\Delta t) = q\int_{-\infty}^{\infty} d\omega \Lambda(\omega) Z(\omega) e^{i\omega \Delta t}. \tag{2.29}$$

This means, that particles will be interacting with be affected by their own induced voltage, and that the induced voltage of “leading” particles w.r.t. t-axis will be experienced by “trailing” particles. Hence, motion of beam particles is coupled, and the interaction of the beam with the impedance of the machine is often referred to as intensity or collective effects.

2.3 BLonD code

For all simulations presented in this thesis, the Beam Longitudinal Dynamics simulation suite BLonD [7] is used. BLonD is a longitudinal macro-particles tracking code for synchrotrons, developed in the BE/RF group at CERN.

2.3.1 Equations of motion

The BLonD simulator is based on the discretised equations of motion presented in Eqs. 2.17 and 2.18, using the coordinates $\Delta t = t - t_s$ and $\Delta E^n = E - E_s$. The absolute reference time at turn n is

$$t_s^n = \sum_{n=1}^{n} T_0^i\,, \tag{2.30}$$

where, as before, the revolution period is defined as $T_0 = \frac{2\pi R_s}{\beta_s c}$ with R_s being the average radius for a given synchronous orbit.

The kick equation assuming K rf systems then reads as [7]:

$$\Delta E^{n+1} = \Delta E^n + \sum_{k=0}^{K-1} V_k^n \sin\phi_{\mathrm{rf},k}(\Delta E^n) - (E_s^{n+1} - E_s^n)\,, \tag{2.31}$$

and the drift equation is given by:

$$\Delta t^{n+1} = \Delta t^n + T_0^{n+1}\left[(1 + \alpha_0^{n+1}\delta^{n+1} + \alpha_1^{n+1}(\delta^{n+1})^2 + \alpha_2^{n+1}(\delta^{n+1})^3\left(\frac{1+\frac{\Delta E^{n+1}}{E_s^{n+1}}}{1+\delta^{n+1}}\right) - 1\right]\,, \tag{2.32}$$

where, instead of the slippage factor, the first three orders in the momentum compaction factor α have been used. The momentum compaction factor is defined as [5]

$$\alpha = \frac{1}{R_s}\frac{dR}{d\delta} = \alpha_0 + 2\alpha_1\delta + 3\alpha_2\delta^2 + \ldots \tag{2.33}$$

and can be related to the slippage factor as follows:

$$\begin{aligned}
\eta_0 &= \alpha_0 - \frac{1}{\gamma_s^2} \\
\eta_1 &= \frac{3\beta_s^2}{2\gamma_s^2} + \alpha_1 - \alpha_0\eta_0 \\
\eta_2 &= -\frac{\beta_s^2(5\beta_s^2 - 1)}{2\gamma_s^2} + \alpha_2 - 2\alpha_0\alpha_1 + \frac{\alpha_1}{\gamma_s^2} + \alpha_0^2\eta_0 - \frac{3\beta_s^2\alpha_0}{2\gamma_s^2}\,.
\end{aligned} \tag{2.34}$$

The momentum compaction factor also determines the relativistic gamma corresponding to the so-called "transition energy",

$$\alpha \equiv \frac{1}{\gamma_t^2} \tag{2.35}$$

Below transition energy ($\gamma < \gamma_t$), a particle with $\delta > 0$ (i.e. a higher-energy particle) has a higher revolution frequency, while above transition energy ($\gamma > \gamma_t$) it has a smaller revolution frequency.

With only a zeroth order momentum compaction factor, the Hamiltonian becomes

$$H(\Delta t, \Delta E) = \frac{\alpha_0 - \frac{1}{\gamma_s^2}}{2\beta_s^2 E_s}(\Delta E)^2 + \sum_{k=0}^{K-1} \frac{qV_k}{T_0\omega_{\mathrm{rf}}^k}\left(\cos(\omega_{\mathrm{rf}}^k \Delta t + \varphi_{\mathrm{rf}}^k) - \cos(\omega_{\mathrm{rf}}^k \Delta t_s + \varphi_{\mathrm{rf}}^k)\right) + \frac{dE_s}{dt}(\Delta t - \Delta t_s)\,. \tag{2.36}$$

3 LHC longitudinal dynamics

This section gives an overview of LHC beam and machine parameters that have been used for the simulations described in this thesis.

3.1 LHC parameters

Table 3.1 summarises the relevant machine parameters, mainly as defined in the LHC Design Report [3]; the value cited for the γ_t is the one that has been in use operationally since 2017.

Table 3.1: LHC machine parameters

Parameters	Symbol	LHC
Circumference	C	26659 m
Gamma transition	γ_t	53.8
Harmonic number	h	35640
Slippage factor	η	3.455×10^{-4}
Revolution frequency	f_{rev}	11245.5 Hz

The cycle of the LHC consists of three phases: the first is injection or “flat bottom”, the second is the acceleration ramp that lasts approximately twenty minutes, and the third phase is “flat top”. During the acceleration phase, both the magnetic field and the RF frequency are ramped. The magnetic field ramp results in a parabolic-exponential-linear-parabolic momentum program as depicted in Fig. 3.1. The RF voltage is programmed to ramp linearly, see Fig. 3.2.

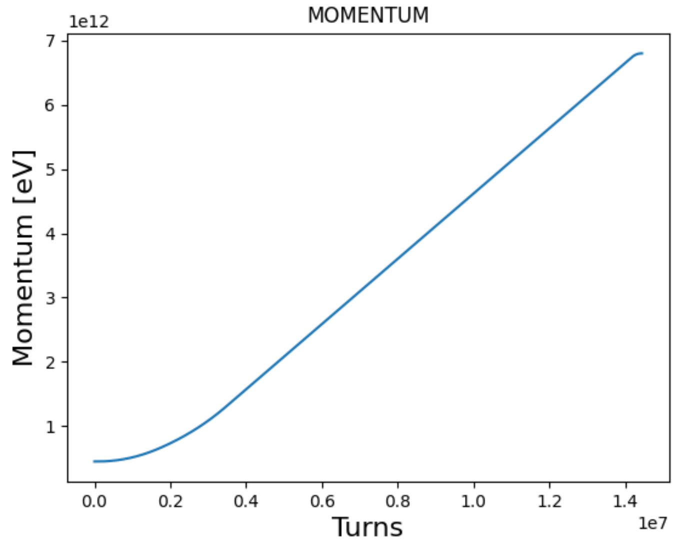

Figure 3.1: Momentum during the LHC ramp with 10000 turns of flat bottom and flat top.

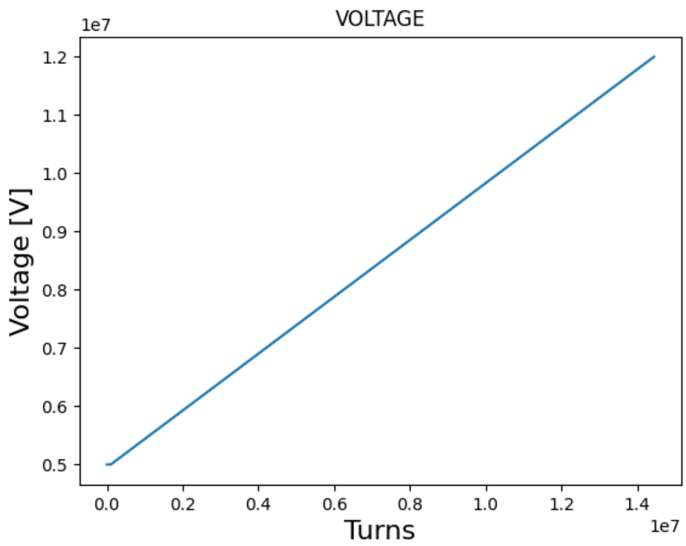

Figure 3.2: An example for the RF voltage program during the LHC ramp with 10000 turns of flat bottom and flat top.

3.2 Toward a High-Luminosity LHC

In general, the quantity that measures the ability of a particle accelerator to produce the required number of collisions per unit time and cross section is called luminosity [8].

Originally, the LHC proton beam energy was designed to be 7 TeV [3] at flat top. However, during the initial operational period of Run 1 (2008-2012), the LHC flat top energy had to be limited to 4 TeV. During Run 2(2015-2018), the energy of the LHC's proton beams was set to reach 6.5 TeV, while for Run3 (starting in 2022) it was increased to 6.8 TeV.

Also, the bunch intensity during Run 1 and Run 2 was limited to the value of 1.3×10^{11} p/b, which was the nominal value according to the original design [3]. The High-Luminosity upgrade of the LHC (HL-LHC) [9] foresees to reach a bunch intensity of 2.3×10^{11} p/b at injection and 2.2×10^{11} p/b at flat top after 2028. In preparation, the LHC injector chain has already been upgraded in 2019-2021 during the LHC Injectors Upgrade (LIU) [10]. In the LHC during Run 3, the plan is to gradually ramp up the intensity to 1.8×10^{11} p/b.

For different intensity ranges, the bunch emittance at SPS extraction has been estimated based on 2018 operational experience and the LIU baseline for HL-LHC bunch intensity [11, 12]. The resulting minimum-maximum expected emittance ranges are shown in Table 3.2, along with the foreseen operational RF voltages.

At injection, the RF cavities are exposed to high beam loading and the RF voltage has to be minimised as much as possible to limit the required RF power to what is available from the LHC klystrons. Table 3.2 shows the minimum injection voltage that allows capturing bunches of a given emittance with acceptable losses, which was scaled from 2018 operational experience, too.

Lastly, the flat top RF voltages are listed. The flat top voltage was determined by scaling 2018 operational values with bunch intensity, keeping the same operational margin to the threshold of single-bunch loss of Landau damping.

Table 3.2: Expected bunch emittances at injection and foreseen operational RF voltage values at flat bottom and flat top during Run 3 and HL-LHC.

Bunch intensity	SPS extraction emittance	Flat bottom voltage	Flat top voltage
$\leq 1.4 \times 10^{11}$ p/b	(0.4-0.48) eVs	5 MV	12 MV
(1.4-1.8)$\times 10^{11}$ p/b	(0.49-0.57) eVs	7 MV	14 MV
(1.8-2.3)$\times 10^{11}$ p/b	0.57 eVs	8 MV	16 MV

3.3 Bunch distribution and profile

The particle distribution in phase space can be different for different modes of operation of an accelerator. For our application, it is convenient to describe the bunch distribution using a binomial with exponent μ as follows:

$$F(J) = F_0 (1 - \frac{J}{J_0})^{\mu}, \tag{3.1}$$

where F_0 is a normalization factor and J_0 is the value of the action J along the trajectory that encloses all particles. This results in the following bunch profile along the longitudinal coordinate t:

$$\lambda(t) = \lambda_0 \left(1 - \left(\frac{t}{\frac{\tau_{\text{full}}}{2}}\right)^2\right)^{\mu+\frac{1}{2}}, \tag{3.2}$$

where τ_{full} is the full bunch length of the distribution and λ_0 is a constant that can be found from the normalization condition

$$\int_{-\infty}^{\infty} \lambda(t) dt = 1. \tag{3.3}$$

Both in machine operation and in simulations, we define the bunch length as a scaled bunch length measurement using the full width at half maximum definition:

$$\tau \equiv \frac{2}{\sqrt{2 \ln 2}} \tau_{\text{FWHM}}. \tag{3.4}$$

For a Gaussian bunch, this definition results in a four-sigma bunch length. For a binomial distribution, the above bunch length definition can be related to the full bunch length as follows:

$$\tau_{\text{full}} = \frac{1}{\sqrt{1 - \frac{1}{2^{1/(\mu+\frac{1}{2})}}}} \frac{\sqrt{2 \ln 2}}{2} \tau. \tag{3.5}$$

The relevant emittance is given from the following equation:

$$\epsilon = \frac{4 E \omega_{s,0} \beta^2}{\omega_{\text{rf}}^2 \eta_0} \int_0^{\phi_b} \sqrt{2(\cos\phi - \cos\phi_b)} d\phi, \tag{3.6}$$

where ϕ_b is the maximum phase of the bunch.

3.4 LHC impedance

In the following simulations presented in this thesis, collective effects are taken into consideration. In order to reproduce the operational conditions, an already existing impedance model for LHC was imported. The impedance model for LHC consists of resistive (real) and inductive (imaginary) parts: $Z = Z_r + i Z_i$. In general, the impedance of a given machine element depends on the geometry and the material of the vacuum enclosure, as well as on the exciting frequency [13]. The LHC impedance model, see Fig. 3.3, includes the contributions from the beam screens in the cold magnets, the vacuum chamber in the warm sections, and a broadband resonator model that takes into account the pumping slots of the beam screens, the experimental chambers, the RF cavities, the Y-chambers, beam instrumentation devices, and the collimators [14].

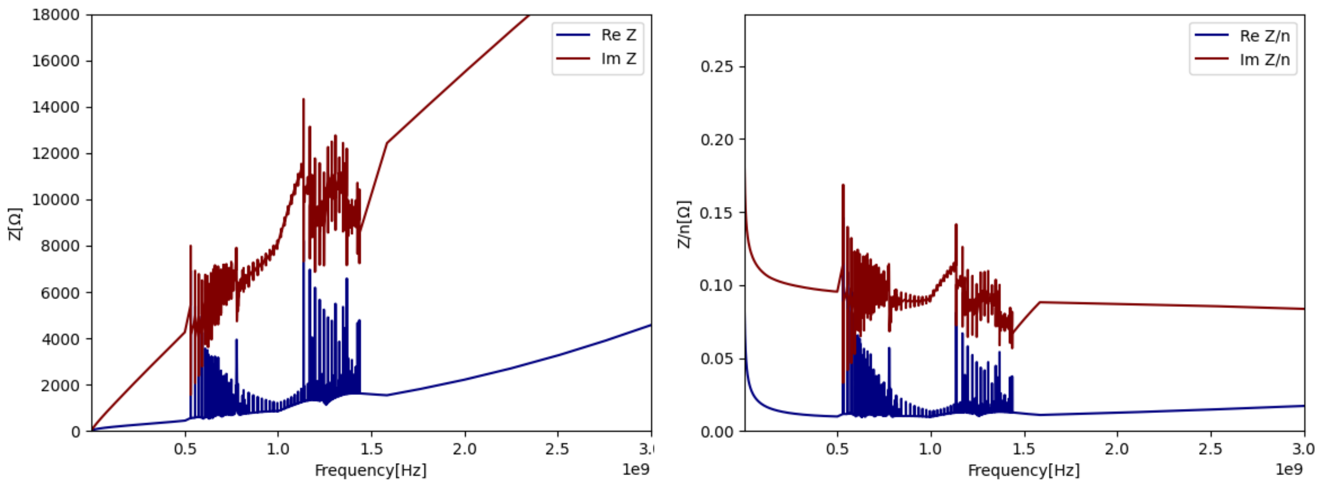

Figure 3.3: Impedance model for LHC at injection (450 GeV). Real (blue) and imaginary (red) part of the LHC impedance model, without scaling (left) and divided by n= ω/ω_0 (right).

3.5 Landau damping

The theory of Landau damping was first derived in the context of plasma physics and it can be defined as follows [15]: the damping of a collective mode of oscillations in plasmas without collisions of charged particles. The damping was predicted by Landau, who deduced this effect from a mathematical study.

In the context of beam dynamics, Landau damping means the suppression of an instability by a spread of frequencies in the beam. It is a very powerful tool at the disposal of accelerator physics that can help to control instabilities [16]. To illustrate Landau damping via a simple example, assume a set of oscillators that each have a different resonant frequency. If a pulsed excitation is given to this system of oscillators, each of them will resonate at a different frequency. Observing the center-of-mass motion of this system, the overall or coherent motion will be smaller than the individual or incoherent motion.

Put in the context of beam physics, Landau damping is present while the spectrum of the excitation source (impedance) overlaps only with the incoherent, continuous beam spectrum, where a spread in frequencies is present and the coherent motion is damped w.r.t. the incoherent motion. Under certain conditions, e.g. as the beam intensity increases, or the bunch length decreases, coherent lines can start to separate from the incoherent beam spectrum; this moment is when Landau damping is lost.

The latest formula for the intensity threshold of loss of Landau damping is [17, 18]:

$$N_{p,\mathrm{th}} = -\frac{\pi V_0 \cos\phi_{s0}\phi_{\max}^5}{32 q h^2 \omega_0 \mu(\mu+1)\chi(k_{\max}\phi_{\max}/h,\mu) Z_{\mathrm{norm}}}, \tag{3.7}$$

where $\phi_{\max} = \omega_{\mathrm{rf}}(\tau_{\mathrm{full}}/2)$, μ is the exponent of the binomial distribution, Z_{norm} is the normalized impedance in units of Ohms and χ is the following hypergeometric function:

$$\chi(y,\mu) = y\left[1 - {}_2F_3(0.5, 0.5; 1.5, 2, \mu; -y^2)\right]. \tag{3.8}$$

3.6 Beam control loops

The low power-level RF system comprises all the electronics that control the RF cavities and the beam motion relative to the RF system. Feedback loops around each cavity, so-called cavity control loops, achieve to keep the RF voltage phase and amplitude in the accelerating cavities as programmed, while beam control loops make sure that the RF frequency and phase seen by the beam is the programmed one and diminish the effect of undesired RF noise [19, 20]. Beam control loops also play an important role when capturing the beam that arrives from another machine. At LHC capture, the beam phase loop makes sure that the RF bucket is centered around the beam, and quickly applies necessary corrections on the RF frequency. The synchronisation loop, acting on a ten times slower time scale, ensures that in the long term the RF frequency stays as programmed. Both loops have been applied for simulations in this thesis and are detailed below.

The beam phase loop is designed to keep the bunches in the center of the RF bucket by measuring the difference between the cavity and the bunch phase and correcting this difference with an RF frequency offset. It is used to damp dipole oscillations and undesired RF noise around the central synchrotron frequency. In this way, it improves significantly the beam lifetime in the LHC. At injection, it also corrects the injection phase and energy errors, and prevents the bunch emittance to blow-up due to these errors. To achieve this, the gain of phase loop is operationally set to be $1/(5T_0)$ and is thus much faster than the synchrotron period ($\mathcal{O}(100T_0)$).

The synchronisation loop is used to measure the difference between the actual and the programmed RF frequency, and corrects it also by applying an RF frequency offset, just as the beam phase loop does. For the two loops not to cancel out each other, the synchronsation loop has to act on a slower time scale; in the LHC, its operational gain is $1/(50T_0)$. Another functionality of the synchronisation loop is, as the name suggests, to synchronise the RF frequency with the SPS at LHC injection.

To demonstrate the combined action of the beam phase and synchronisation loops, we present a simple simulation of a single bunch being captured with an energy or phase error at injection. Figure 3.4 shows the center of mass (COM) motion after an initial energy offset of 76 MeV (left) and a time offset of 0.5 ns (right).

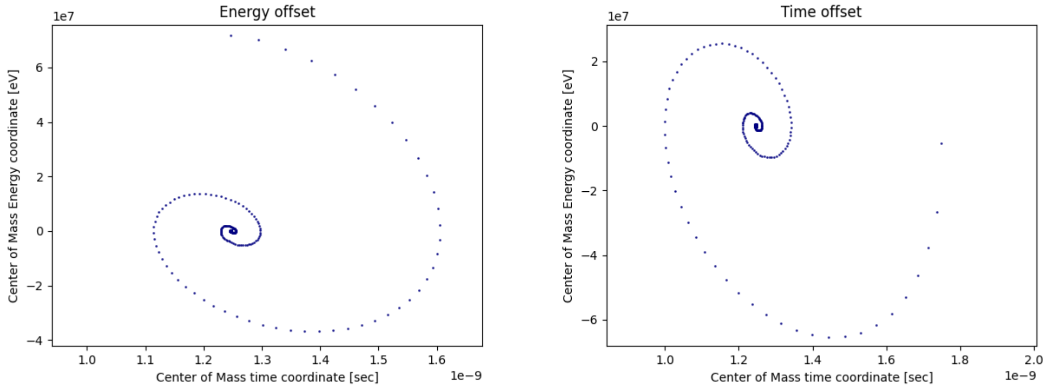

Figure 3.4: Simulated COM motion of a single bunch injected into the LHC with an energy offset of 76 MeV (left) and a time offset of 0.5 ns (right), in the presence of the beam phase and synchronisation loops. Each dot represents the COM position at consecutive turns at and after injection.

As we can see from the COM motion, the beam control loops manage to pull back the bunch to the center of the bucket within a few tens of turns; at injection, the bucket center is $(\Delta t, \Delta E) = (T_{\mathrm{rf}}/2, 0)$ based on the equations of motion.

Combining the above energy and phase errors results in phase space in a significant offset of the bunch w.r.t. the rf bucket, as shown in Fig. 3.5 (top). If uncorrected, these injection errors would lead to significant particle losses. Thanks to the beam control loops, however, the losses are minimised and the bunch re-centered, see Fig. 3.5 (bottom).

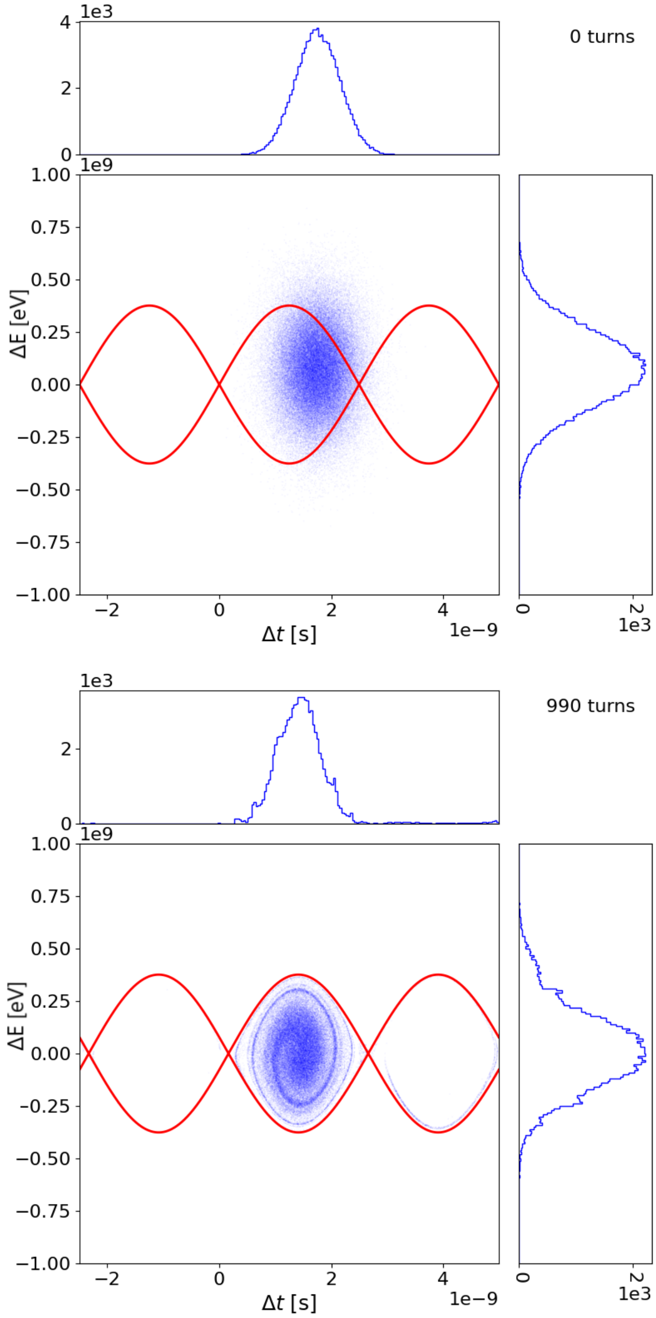

Figure 3.5: Phase-space distribution at injection (top) and after 990 turns (bottom) in the presence of beam phase and synchronisation loops, and after an initial injection error of 0.5 ns in phase and 76 MeV in energy.

4 Single-bunch instabilities during the acceleration ramp

In this chapter, single bunches are simulated using the BLonD code during the acceleration ramp. Collective effects are included by using the LHC impedance model at injection. No beam control loops or RF noise is being applied in these simulations. The aim was to determine under what operational conditions single-bunch instability would occur in the absence of beam control loops, natural RF noise and controlled emittance blow-up. Due to the computationally heavy simulations, single-bunch motion including collective effects during the LHC ramp has not been systematically studied in simulations before, and only became possible through recent runtime improvements of the BLonD code [21].

4.1 Simulation conditions

To cover the operational ranges of Run 3 and HL-LHC in terms of bunch parameters, 36 different combinations of bunch length and intensity were simulated, see Table 4.1. Furthermore, the LHC machine parameters as listed in Table 3.1 were used, with an acceleration ramp from 450 GeV to 6.5 TeV as shown in Fig. 3.1. For the RF voltage, a linear ramp from 6 MV to 12 MV was assumed.

Table 4.1: Initial bunch parameters: 36 combinations of the below bunch lengths and intensities were used in the simulations.

Bunch length[ns]	Intensity[$\times 10^{11}$p/b]
1.1	1.1
1.2	1.4
1.3	1.8
1.4	2.1
1.5	2.3
1.6	2.6

The initial phase-space distribution of the bunch was generated in BLonD using a routine that matches the distribution function to the potential well. To do so, the routine generates a beam according to the distribution function and bunch emittance chosen by the user. The potential well is calculated as the sum of the RF potential and the induced potential from the impedance; numerically, it is pre-processed to look for a global minimum within a given frame specified by the user. For the bunch distributions in this thesis, a binomial distribution with an exponent of $\mu = 1.5$ has been assumed, as it describes well on average the operationally observed bunch profiles.

Figure 4.1 shows an example of the phase-space distributions of the bunch at flat bottom and flat top. As we can see, at flat bottom the height of the bucket is around 400 MeV, while at flat top it is around 2 GeV. As the bunch preserves its emittance, unless an instability occurs, its bunch length is shrinking constantly during the acceleration ramp.

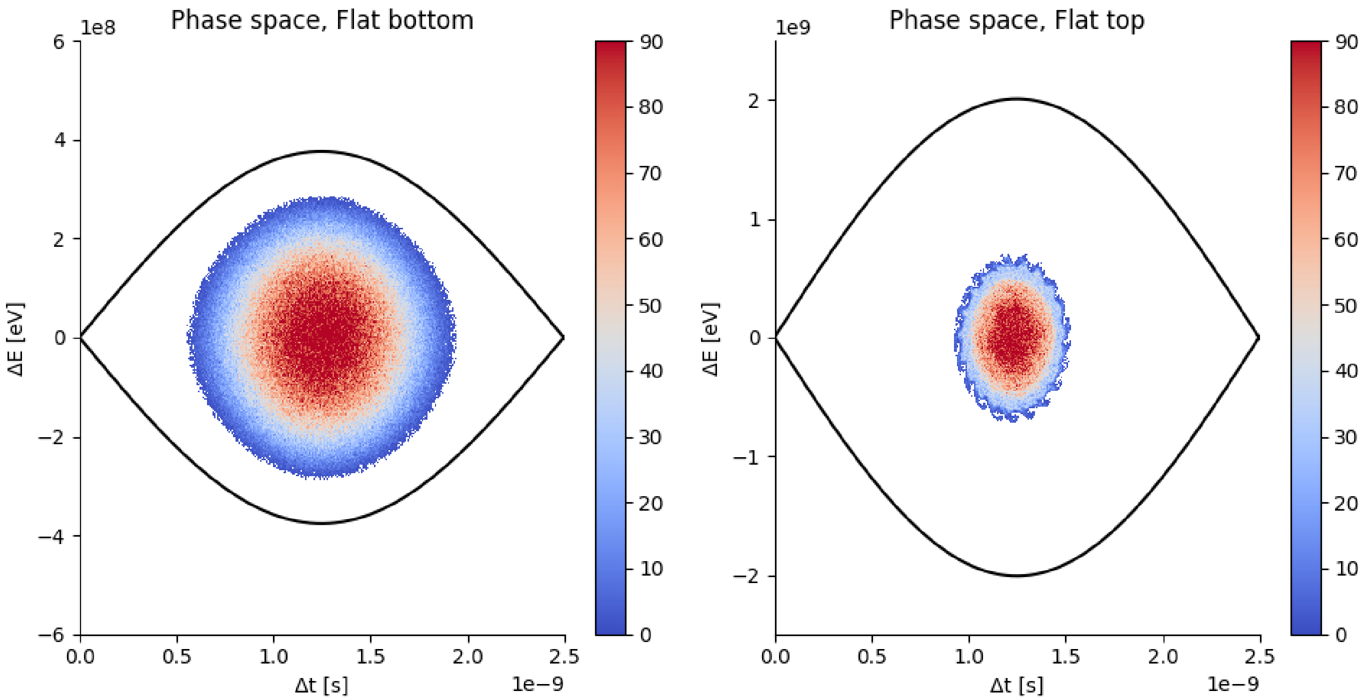

Figure 4.1: Phase space plots at the start (left) and at the end of the simulation (right). An example for a bunch with an intensity of 1.1×10^{11} p/b and an initial bunch length of 1.2 ns.

4.2 Adiabatic bunch length decrease

Neglecting intensity effects, the Hamiltonian shown in Eq. 2.19 is a conservative function. This means, that the bunch emittance is preserved while the energy and voltage are increasing during the acceleration ramp. As a result, the bucket area increases and the bunch length decreases. In a single-harmonic RF system, the maximum phase can be calculated as [5]:

$$\phi_{\max} = hA^{1/2}\left(\frac{\omega_0}{\pi\beta_s^2 E_s}\right)^{1/2}\left(\frac{2\pi\beta_s^2 E_s|\eta|}{heV|\cos\phi_s|}\right)^{1/4}. \tag{4.1}$$

from which we can conclude that in an adiabatic ramp, the bunch length will scale with voltage and energy as follows:

$$\tau \propto \frac{1}{(VE_s)^{1/4}}. \tag{4.2}$$

4.3 Simulation results

An example of the bunch length evolution throughout the ramp, starting from a 1.2 ns bunch length but different intensities is shown in Figs. 4.2 and 4.3; the simulation data is shown in blue. For comparison, the adiabatic bunch length shrinking based on Eq. 4.2 is plotted in purple.

Initially, the bunch length behaviour is well described by the adiabatic curve. However, the simulations take into account collective effects, so the bunch length is not necessarily expected to shrink adiabatically. After a few million turns already, a slight and smooth increase of the bunch length can be observed compared to the adiabatic prediction. Towards the higher energies, eventually, the bunch length blows up in an uncontrolled way: the bunch length spread increases, the bunch length itself has fluctuations and the final bunch length at flat top strongly deviates from the adiabatic value; the bunches become unstable. Comparing different intensities, one can also observe that for lower intensities the instability starts later for the same initial bunch length, and the blow-up is more violent. While, for higher intensity, the blow-up starts earlier and the rise of the bunch length is "smoother".

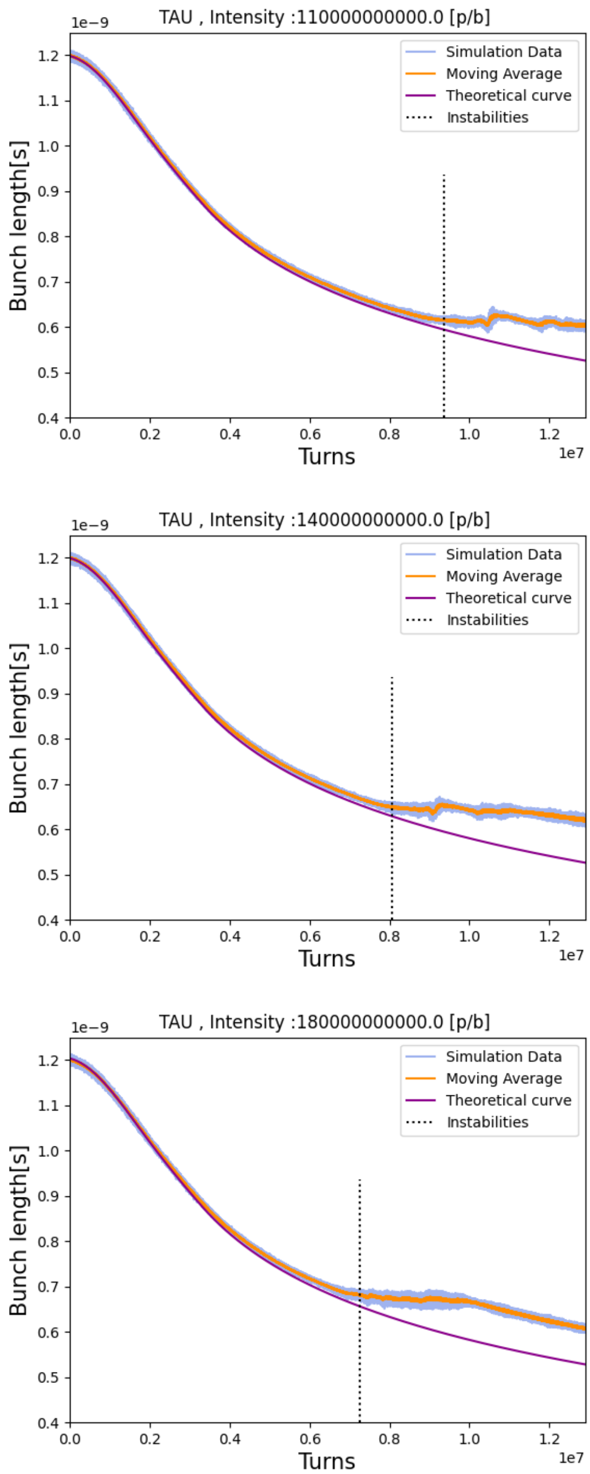

Figure 4.2: Bunch length evolution during the LHC ramp with an initial bunch length of 1.2 ns, for intensities of 1.1×10^{11} p/b (top), 1.4×10^{11} p/b (middle), and 1.8×10^{11} p/b (bottom). The simulation data (blue) and its smoothed value using a moving average (orange) are plotted from the BLonD results, the adiabatic behaviour (purple) is based on Eq. 4.2.

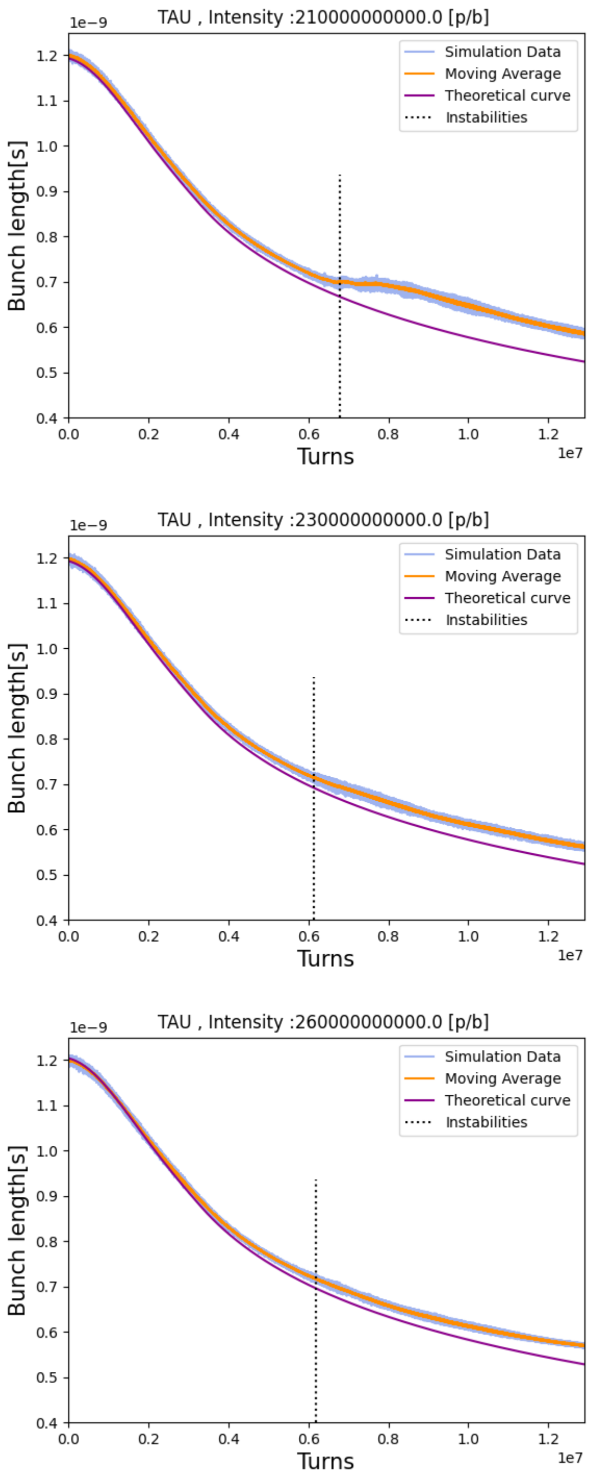

Figure 4.3: Bunch length evolution during the LHC ramp with an initial bunch length of 1.2 ns, for intensities of 2.1×10^{11} p/b (top), 2.3×10^{11} p/b (middle), and 2.6×10^{11} p/b (bottom). The simulation data (blue) and its smoothed value using a moving average (orange) are plotted from the BLonD results, the adiabatic behaviour (purple) is based on Eq. 4.2.

In order to find the exact turn at which the instability occurred, we analyse the bunch length oscillations for each case. The oscillation amplitude for each turn was calculated as the difference between the maximum and the minimum value of the bunch length within 100 turns. Then, looking at the evolution of the oscillation amplitude for each case, a suitable threshold was defined and a bunch was considered to be unstable when the oscillations rose above that threshold. The threshold that would fit all the cases was found to be the initial value of the bunch length oscillation $+0.17 \times 10^{-11}$ s.

An example is shown in Fig. 4.4. According to our threshold definition, in the top plot no

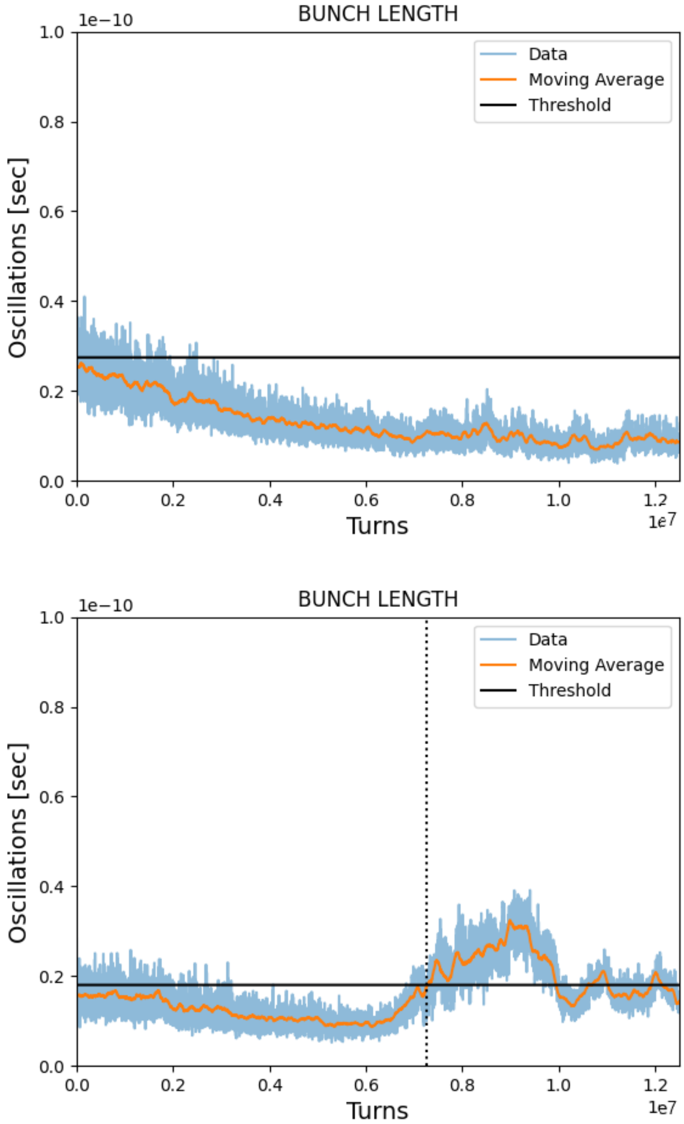

Figure 4.4: Oscillations for intensity: 1.1×10^{11} [p/b] and 1.8×10^{11} [p/b] and bunch length: 1.5 [nsec], 1.2[nsec]

instability is detected, since the oscillations are always below the threshold. Instead, in the bottom plot the threshold is overcome at turn 6784820, which coincides with the start of an uncontrolled blow-up of the bunch length. The rest of the cases are presented in Appendix A.

Tables 4.2 through 4.7 summarize the cases in which instabilities occurred; the rest cases that are not listed in these tables were stable. The tables show the turn number at which the instability was detected, along with the full bunch length, energy, and voltage at the moment of the instability.

Table 4.2: Instabilities for an intensity of 1.1×10^{11} p/b

		At the moment of instability			
Intensity	Initial τ	τ_{full}	Turn	Energy	Voltage
1.1×10^{11} p/b	1.1 ns	0.621 ns	7140450	3.23 GeV	9.1 MV
	1.2 ns	0.617 ns	9357690	4.36 GeV	10.1 MV

Table 4.3: Instabilities for an intensity of 1.4×10^{11} p/b

		At the moment of instability			
Intensity	Initial τ	τ_{full}	Turn	Energy	Voltage
1.4×10^{11} p/b	1.1 ns	0.6603 ns	6152870	2.72 GeV	8.68 MV
	1.2 ns	0.651 ns	8051610	3.69 GeV	9.5 MV

Table 4.4: Instabilities for an intensity of 1.8×10^{11} p/b

		At the moment of instability			
Intensity	Initial τ	τ_{full}	Turn	Energy	Voltage
1.8×10^{11} p/b	1.1 ns	0.6774 ns	5720000	2.52 GeV	8.52 MV
	1.2 ns	0.6896 ns	7246000	3.3 GeV	9.2 MV
	1.3 ns	0.6736 ns	9872420	4.66 GeV	10.36 MV
	1.4 ns	0.6891 ns	10650000	4.77 GeV	10.46 MV

Table 4.5: Instabilities for an intensity of 2.1×10^{11} p/b

		At the moment of instability			
Intensity	Initial τ	τ_{full}	Turn	Energy	Voltage
2.1×10^{11} p/b	1.1 ns	0.7201 ns	4760000	2.03 GeV	8.1 MV
	1.2 ns	0.7049 ns	6784820	3.07 GeV	8.99 MV
	1.3 ns	0.685 ns	9306350	4.37 GeV	10.11 MV
	1.4 ns	0.699 ns	10650000	5.059 GeV	10.71 MV

As we can observe from Tables 4.2 through 4.7, the instability threshold is influenced by the bunch intensity and the initial bunch length. To be more specific, the larger the initial bunch length, the later the instabilities develop. Inversely, the higher the bunch intensity, the earlier the instabilities appear. In order to analyse these dependencies further, we plotted the scaled

Table 4.6: Instabilities for an intensity of 2.3×10^{11} p/b

		At the moment of instability			
Intensity	Initial τ	τ_{full}	Turn	Energy	Voltage
2.3×10^{11} p/b	1.1 ns	0.729 ns	4580000	1.91 GeV	7.99 MV
	1.2 ns	0.7139 ns	6125000	2.73 GeV	8.7 MV
	1.3 ns	0.7113 ns	8250000	3.82 GeV	9.64 MV
	1.4 ns	0.70608 ns	10280000	4.869 GeV	10.54 MV
	1.5 ns	0.7081 ns	11650000	5.57 GeV	11.15 MV

Table 4.7: Instabilities for an intensity of 2.6×10^{11} p/b

		At the moment of instability			
Intensity	Initial τ	τ_{full}	Turn	Energy	Voltage
2.6×10^{11} p/b	1.1 ns	0.7507 ns	4230000	1.75 GeV	7.87 MV
	1.2 ns	0.7149 ns	6197736	2.74 GeV	8.7 MV
	1.3 ns	0.72655 ns	7300000	3.33 GeV	9.22 MV
	1.4 ns	0.7279 ns	9146000	4.28 GeV	10.04 MV
	1.5 ns	0.7224 ns	9146000	5.56 GeV	11.14 MV

instability threshold $N_{p,\mathrm{th}}/(V\cos\phi_{s0})$ as a function of τ_{full} at the moment when the instability occurred in Fig. 4.5. Unstable cases are marked with purple dots and stable cases with red crosses. The fact that stable and unstable cases clearly separate but lie close to each other shows that our threshold criterion works well and consistently for all the cases.

In the Fig. 4.6 we compare the simulation data to the threshold of loss of Landau damping as defined in Eq 3.7. Although the overall trend is similar for both simulations and theory, the threshold of loss of Landau damping is lower by approximately a factor five. The interpretation is that, indeed, the emergence of the instability and the threshold of loss of Landau damping cannot be directly compared. In the absence of excitation, bunches can stay stable even above the threshold of loss of Landau damping, and it takes time for an instability to develop. In simulations, often the presence of numerical noise is considered to be sufficient to “seed” the instability. On the other hand, in our simulations, no other sources of excitation such as natural RF noise have been modelled, so it is possible that the instabilities are only weakly seeded. Therefore, the threshold of the instability can be much higher than the actual threshold of loss of Landau damping. In fact, in some of the simulated cases, Eq. 3.7 even predicts that Landau damping is already lost at injection. This could also explain why the bunch length starts to deviate from the adiabatic curve already at low energies and gently blows up much before any instability is detected.

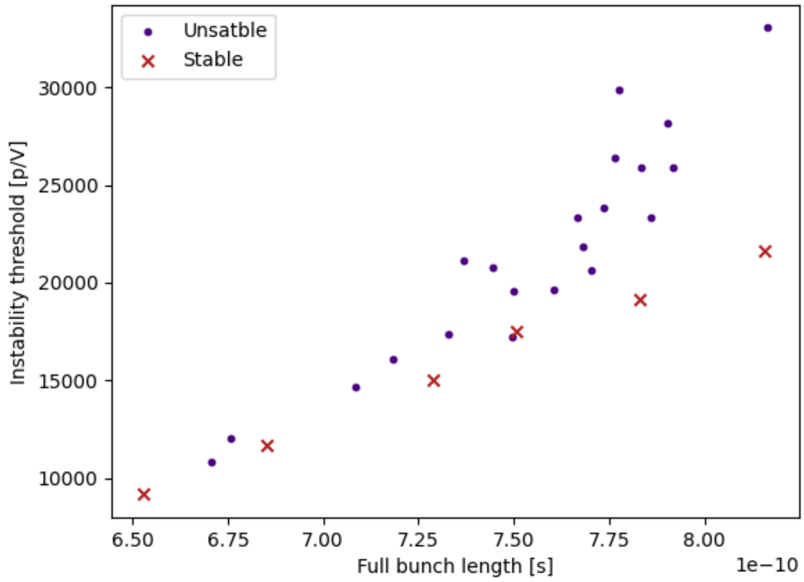

Figure 4.5: Threshold for instabilities that occurred during the acceleration ramp.

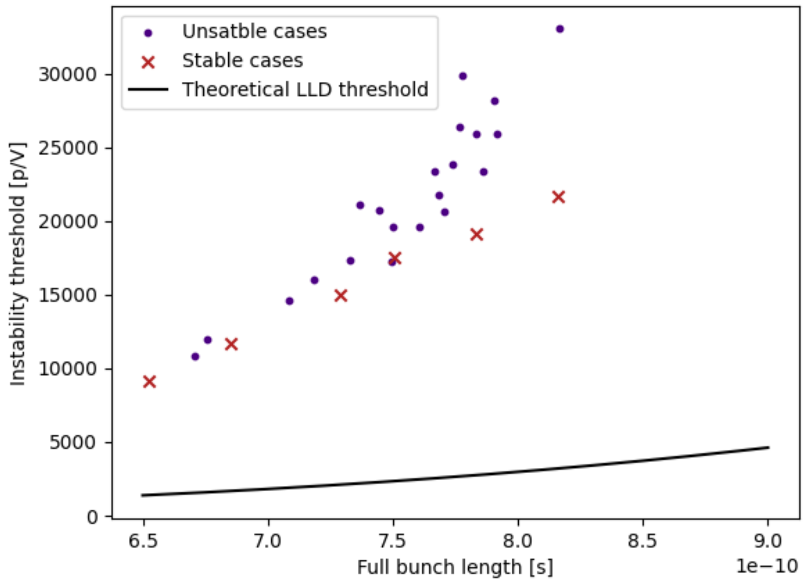

Figure 4.6: Simulated instability threshold compared to the threshold for loss of Landau damping.

5 Controlled emittance blow-up

In this chapter, simulations of single-bunch evolution during the LHC acceleration ramp with controlled emittance blow-up are presented. As we have seen in the previous chapter, controlled blow-up is required to prevent longitudinal instabilities from occurring.

Just as in operation, the blow-up is achieved also in simulation by injecting RF phase noise through the beam phase loop; the synchronisation loop is modelled as well. Simulations of controlled blow-up have been conducted in the past already [22], but neglecting collective effects, for Run 2 intensities only, and without performing parameter scans. The LHC ramp simulations are computationally expensive, since the average runtime per simulation was 1 day with the latest, heavily-optimized BLonD version. A central question is whether the operational method is applicable also in a reproducible way for HL-LHC intensities.

5.1 Noise generation

Controlled emittance blow-up can be obtained by diffusion due to RF phase noise injection [23]. In order to diffuse only particles in the core of the bunch, without creating losses, the spectrum of the phase noise can be targeted to excite the synchrotron frequencies close to the central synchrotron frequency f_{s0}, see Fig. 5.1. In the LHC, the operationally used noise band is $(0.8571-1.05)f_{s0}$, and although there are no particles with a frequency above $1.0f_{s0}$, the spectrum is expanded for the numerical generation of the noise. Within this frequency band, the aim is to excite all particles equally and thus have a flat noise spectrum.

In practise, the noise has to be injected through the beam phase loop for it to be seen by the beam. However, the beam phase loop is exactly designed to counteract RF noise around the synchrotron frequency. In other words, the phase loop has a transfer function with a strong response close to the frequencies around $f_{s,0}$ and partially counteracts the RF phase noise injected on purpose [24]. Thus, to achieve an effective noise spectrum that is flat, the response of the phase loop has been calculated and its inverse has been used to shape the noise spectrum as presented in Fig. 5.2; this is the noise spectrum that is used both in

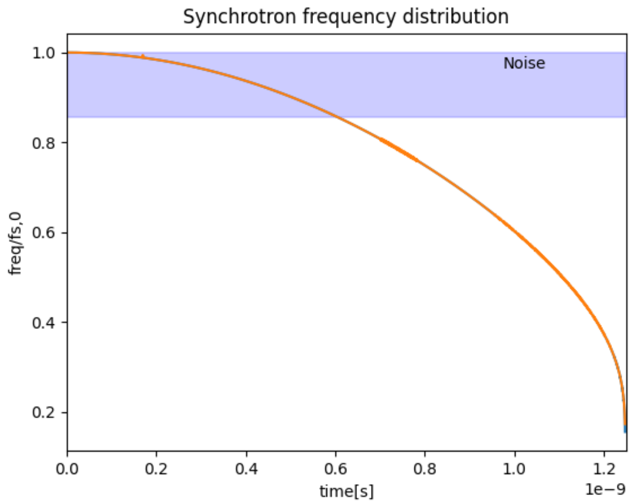

Figure 5.1: Synchrotron frequency distribution in a single-RF system as a function of the time coordinate. The blue region marks the frequency range targeted by the injected phase noise.

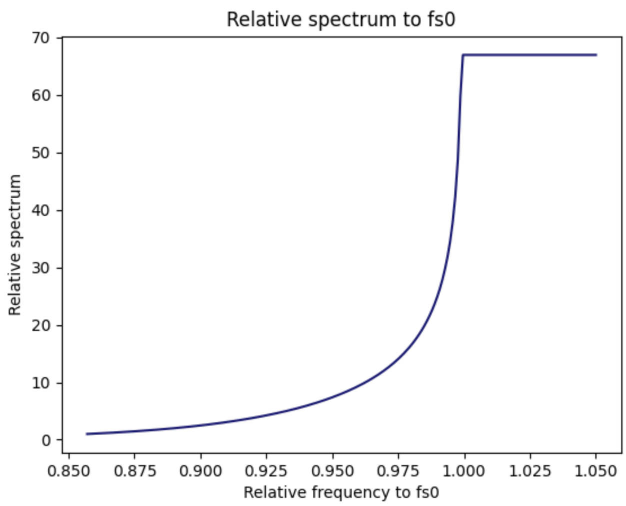

Figure 5.2: RF phase noise spectrum used for controlled emittance blow-up as a function of relative frequency f/f_{s0}.

LHC operation and BLonD simulations. The numerical algorithm for the noise generation is described in [25].

The amplitude of the noise spectrum is regulated by a bunch length feedback that regularly (every 2 s) measures the bunch length τ, compares it to a target bunch length value τ_{targ}, and regulates the noise amplitude x based on a recursive algorithm [24]:

$$x_{n+1} = \alpha x_n + g(\tau_{\text{targ}} - \tau_n), \tag{5.1}$$

where $\alpha = 0.93$ is a "memory" factor and g is a gain that is increased during the ramp proportionally to f_{s0}^2. Every x_{n+1} is limited to the range $[0,1]$. In all simulations, the target bunch length has been 1.2 ns constant throughout the ramp.

5.2 Simulation conditions

For the simulations presented in this chapter, the operationally expected conditions have been simulated for Run 3 and HL-LHC, as summarized in Table 3.2 earlier. The parameter range explored in the simulations is summarized in Table 5.1. In all cases, the flat top energy was assumed to be 6.8 TeV.

Table 5.1: Simulation parameters for Run 3 and HL-LHC conditions. For different bunch intensities, different bunch lengths are considered to be achievable in the SPS at extraction (estimated minimum and maximum values are given). Also the SPS extraction voltages for the main 200 MHz and the fourth-harmonic 800 MHz system were assumed to be different. The LHC flat bottom and flat top voltages were assumed to be the same as in Table 3.2.

	SPS extraction			LHC flat bottom	LHC flat top
Intensity	Bunch lengths	V_{200}	V_{800}	V_{400}	V_{400}
1.1×10^{11} p/b	1.5 ns, 1.65 ns	7 MV	0.7 MV	5 MV	12 MV
1.4×10^{11} p/b	1.5 ns, 1.65 ns	7 MV	0.7 MV	5 MV	12 MV
1.4×10^{11} p/b	1.52 ns, 1.65 ns	10 MV	1 MV	7 MV	14 MV
1.8×10^{11} p/b	1.52 ns, 1.65 ns	10 MV	1 MV	7 MV	14 MV
2.3×10^{11} p/b	1.65 ns	10 MV	2 MV	8 MV	16 MV
2.6×10^{11} p/b	1.65 ns	10 MV	2 MV	8 MV	16 MV

The three different sets of RF voltages during the LHC ramp result in different synchrotron frequencies, and therefore different noise spectra, see Fig. 5.3.

To generate realistic bunch distributions, the distribution has been matched (using the same function as in Chap. 4) at SPS flat top assuming double-harmonic RF and collective effects. As before, a binominal distribution with an exponent of $\mu = 1.5$ has been used. The latest model of the SPS machine impedance has been used, see Fig. 5.4.

Although the LHC voltage at injection is kept as low as possible to limit RF power consumption, it is still larger-than-matched in order to limit beam losses. Therefore, the bunch filaments after injection into the LHC and ends up with a shorter bunch length at the start of the ramp than it had at injection, see Fig. 5.5. The bunch lengths and emittances at SPS extraction and in the LHC after filamentation for the different simulated cases are summarized in Table 5.2.

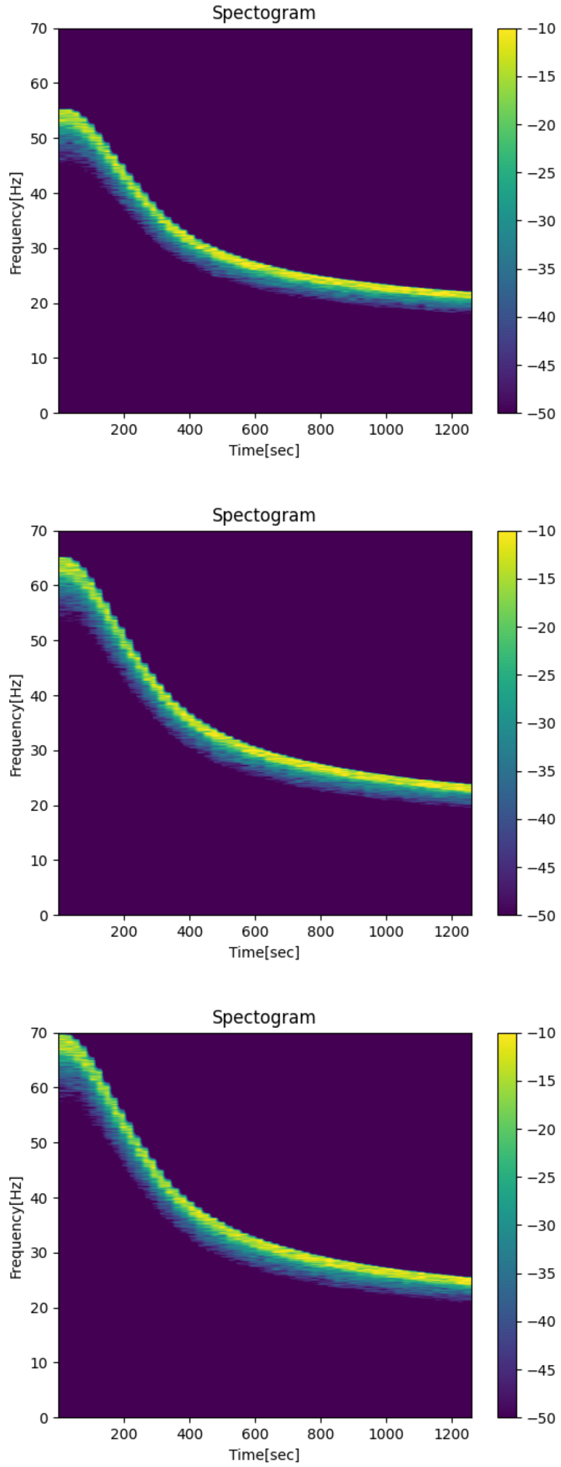

Figure 5.3: Spectrograms for the injected RF phase noise, for the acceleration ramps from 5-12 MV (top), 7-14 MV (middle), and 8-14 MV (bottom).

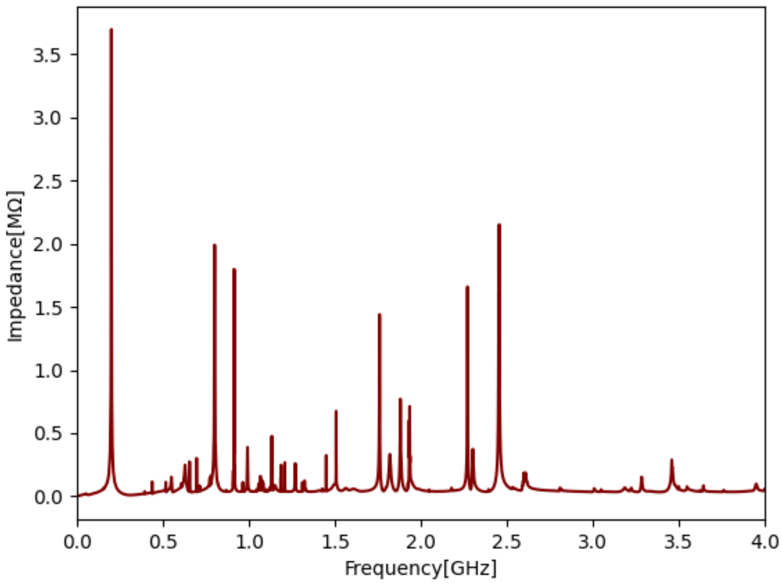

Figure 5.4: Absolute value of the SPS impedance as a function of frequency.

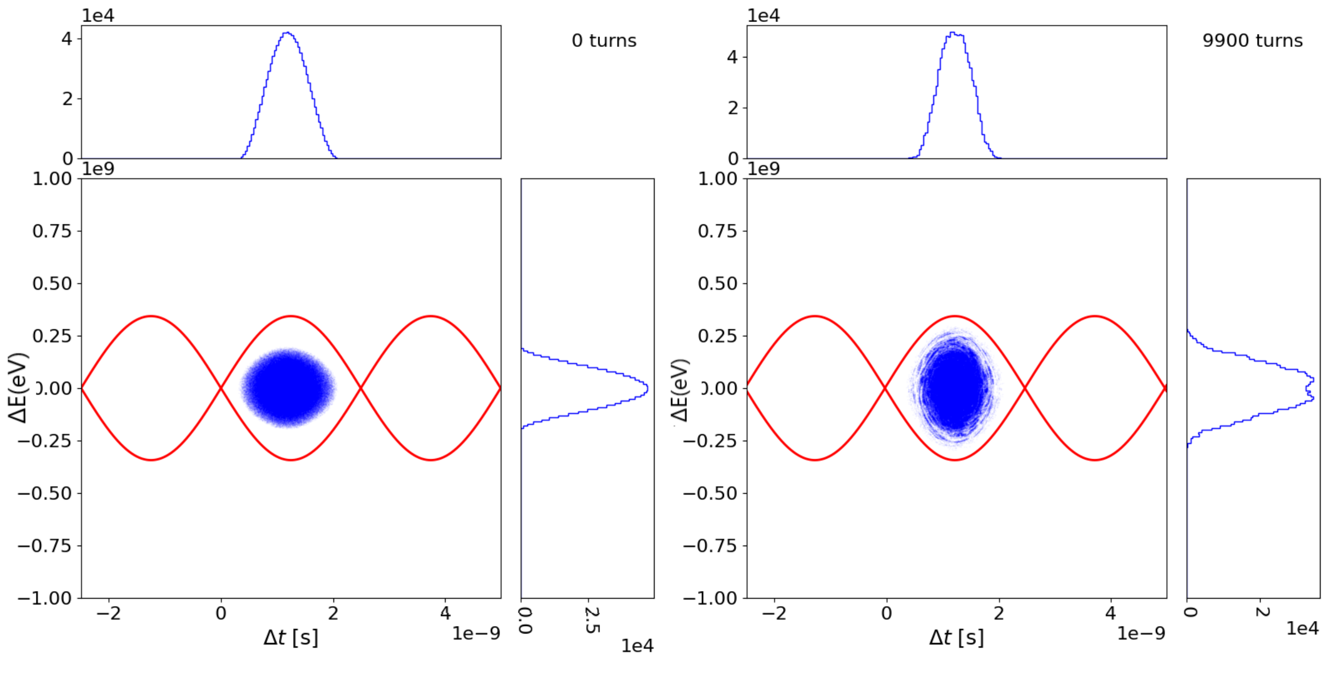

Figure 5.5: Capture of SPS bunches in the LHC: phase-space plots right at the injection (left) and after the filamentation on flat bottom (right).

Table 5.2: Bunch parameters at SPS extraction and in the LHC after filamentation

Intensity	SPS, at extraction τ_{SPS}	ϵ_{SPS}	LHC, after filamentation τ_{LHC}	ϵ_{LHC}	LHC injection V_{400}
1.1×10^{11} p/b	1.5 ns	0.4 eVs	1.167 ns	0.41 eVs	5 MV
1.1×10^{11} p/b	1.65 ns	0.48 eVs	1.277 ns	0.482 eVs	5 MV
1.4×10^{11} p/b	1.5 ns	0.4 eVs	1.162 ns	0.41 eVs	5 MV
1.4×10^{11} p/b	1.65 ns	0.48 eVs	1.195 ns	0.48 eVs	5 MV
1.4×10^{11} p/b	1.52 ns	0.49 eVs	1.186 ns	0.5 eVs	7 MV
1.4×10^{11} p/b	1.65 ns	0.57 eVs	1.282 ns	0.57 eVs	7 MV
1.8×10^{11} p/b	1.52 ns	0.49 eVs	1.177 ns	0.49 eVs	7 MV
1.8×10^{11} p/b	1.65 ns	0.57 eVs	1.188 ns	0.5 eVs	7 MV
2.3×10^{11} p/b	1.65 ns	0.57 eVs	1.321 ns	0.64 eVs	8 MV
2.6×10^{11} p/b	1.65 ns	0.57 eVs	1.303 ns	0.64 eVs	8 MV

5.3 Simulation results

The simulations have been performed with 1 million particles, which proved to be sufficient to obtain converged results independent of the simulation particles used.

An example of the phase space distribution at the start and end of the ramp is given in Fig. 5.6. As the RF noise targets the bunch core, no significant losses were expected. Indeed, during the ramp only a few particles were lost. In the example of Fig 5.6, 993864 particles are left inside the separatrix at the end of the simulation, which means that only 0.614% of the total amount of particles is lost. In general, during the controlled emittance blow-up, an empty area forms between the bunch and the bucket in phase space, so the small amount of losses occurs mainly during the initial phase of the blow-up and virtually no losses are expected at higher energies.

The bunch profiles for each case before the start of the ramp and after the acceleration ramp are presented in Fig. 5.7. As one can observe, the core of the profiles gets rounder during the blow-up, as intended. Also, some shoulders are formed and are visible in the flat top profile. This is reasonable, since in the numerically generated noise spectrum there is some small non-zero spectral density at frequencies below the targeted band and also the diffused particles are driven out towards the bunch tails. However, these shoulders remain small, and in bunch profile measurements in the machine they would be close to the limit of what can be resolved within the typical dynamic range of an oscilloscope.

As mentioned before, we defined the target bunch length to be 1.2 ns constant throughout the ramp. This was motivated by two reasons. Firstly, in order to maintain the same operational margin at flat top from the threshold of loss of Landau damping as in the past, even with the maximum available RF voltage of 16 MV the minimum bunch length that is required at HL-LHC intensities is 1.2 ns. Secondly, the main LHC experiments where the beams from LHC

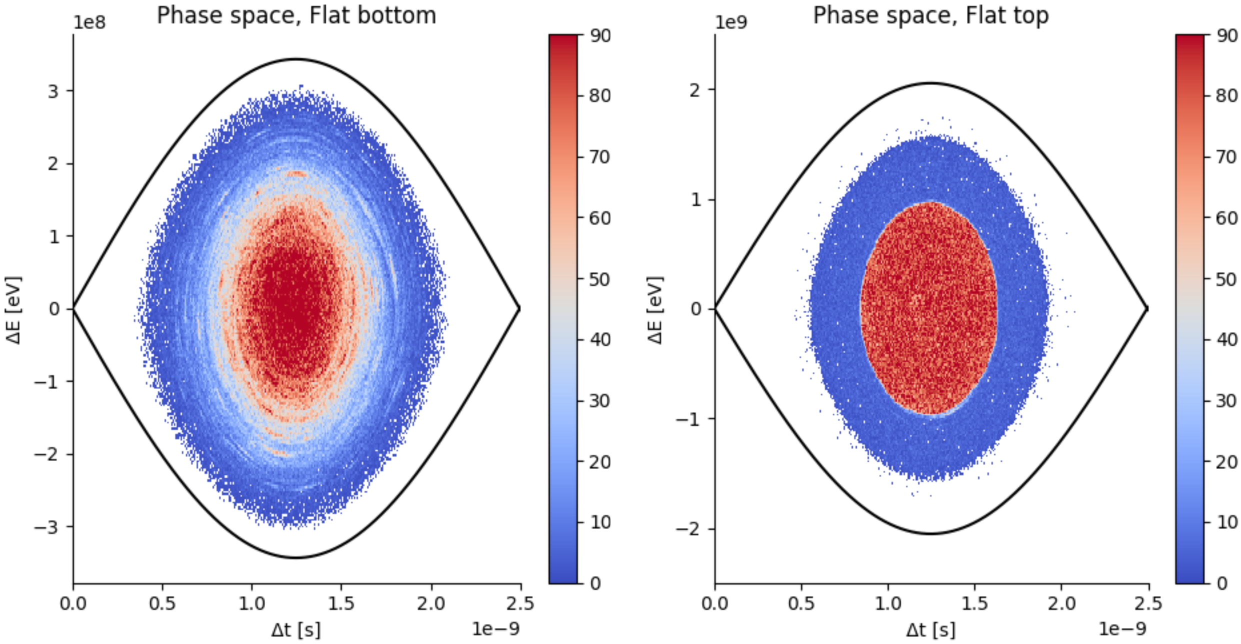

Figure 5.6: Phase space plots at the beginning (left) and at the end of the ramp (right). An example for the intensity of 1.1×10^{11} p/b and an SPS bunch length of 1.5 ns.

are collided are designed for this bunch length and demand for the HL-LHC era bunch lengths in the range of 1.2-1.3 ns at arrival to flat top.

Table 5.3 summarizes for all the simulated cases the initial bunch length after filamentation (after 10000 turns of flat bottom) and the final bunch length achieved using the blow-up at arrival to flat top. As we can see, the bunch length can be regulated well for all intensities and initial bunch lengths simulated. Due to the regulation mechanism of the bunch length feedback, the final bunch length is always somewhat below the target value, around 50 ps for the simulated cases, which agrees well with operational experience.

Figures 5.8 through 5.12 show the bunch length evolution (left) and the noise amplitude x applied by the bunch length feedback (right), for different simulated intensities and an SPS extraction bunch length 1.65 ns in all cases. In the initial 10000 turns, the bunch is kept at flat bottom to filament and to match to the LHC bucket; on the bunch length evolution, this stage is seen as an initial period of oscillation. After that, if the bunch length is above the target value, it will first shrink adiabatically while the noise is off ($x = 0$).

Then, while the noise level is being increased (i.e. x is increasing), the bunch length often goes through some sudden increase or jumps. In the presented results, these jumps are limited to 100 ps in amplitude, while in operation overshoots of 400-500 ps have been observed. Surprisingly, as the intensity increases, these jumps are less and less observed and bunch length regulation on average becomes smoother. Towards the second half of the ramp, the

Table 5.3: Bunch length before and after the LHC ramp with controlled emittance blow-up.

Intensity	Initial bunch length	Final bunch length	Voltage
1.1×10^{11} p/b	1.167 ns	1.162 ns	5-12 MV
1.1×10^{11} p/b	1.277 ns	1.153 ns	5-12 MV
1.4×10^{11} p/b	1.162 ns	1.147 ns	5-12 MV
1.4×10^{11} p/b	1.195 ns	1.194 ns	5-12 MV
1.4×10^{11} p/b	1.186 ns	1.144 ns	7-14 MV
1.4×10^{11} p/b	1.282 ns	1.149 ns	7-14 MV
1.8×10^{11} p/b	1.177 ns	1.149 ns	7-14 MV
1.8×10^{11} p/b	1.188 ns	1.149 ns	7-14 MV
2.3×10^{11} p/b	1.321 ns	1.152 ns	8-16 MV
2.6×10^{11} p/b	1.303 ns	1.149 ns	8-16 MV

noise amplitude is more stable in all cases, and the average bunch length is well maintained close to the target value. However, as one can observe, the turn-by-turn bunch length data is very noisy and the peak-to-peak excursions in bunch length increase with intensity.

Globally, in any case, we can conclude that in simulations the presently used operational method for controlled emittance blow-up in the LHC works well up to HL-LHC intensities for single bunches.

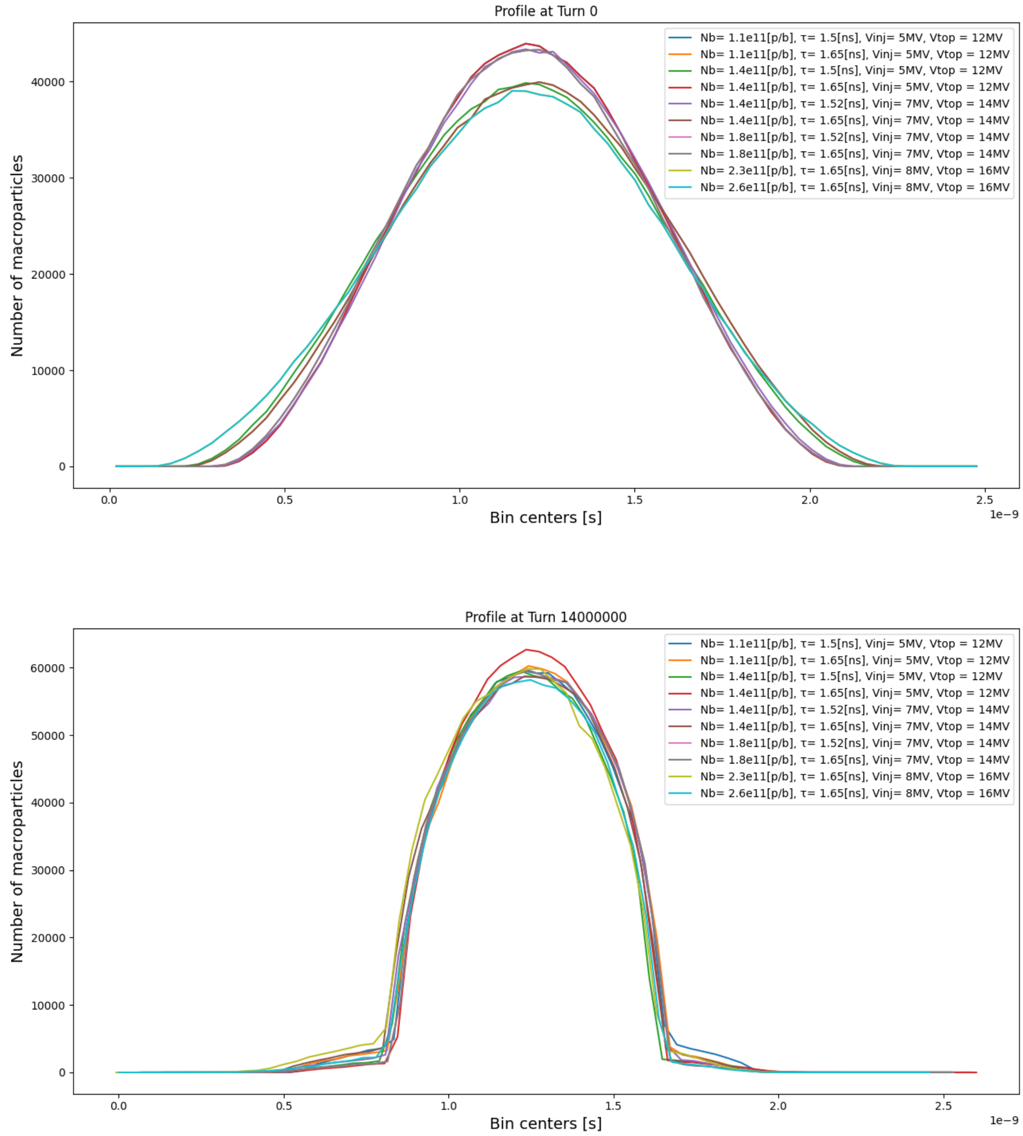

Figure 5.7: Bunch profiles at the beginning (top) and at the end of the ramp (bottom) for all simulated cases.

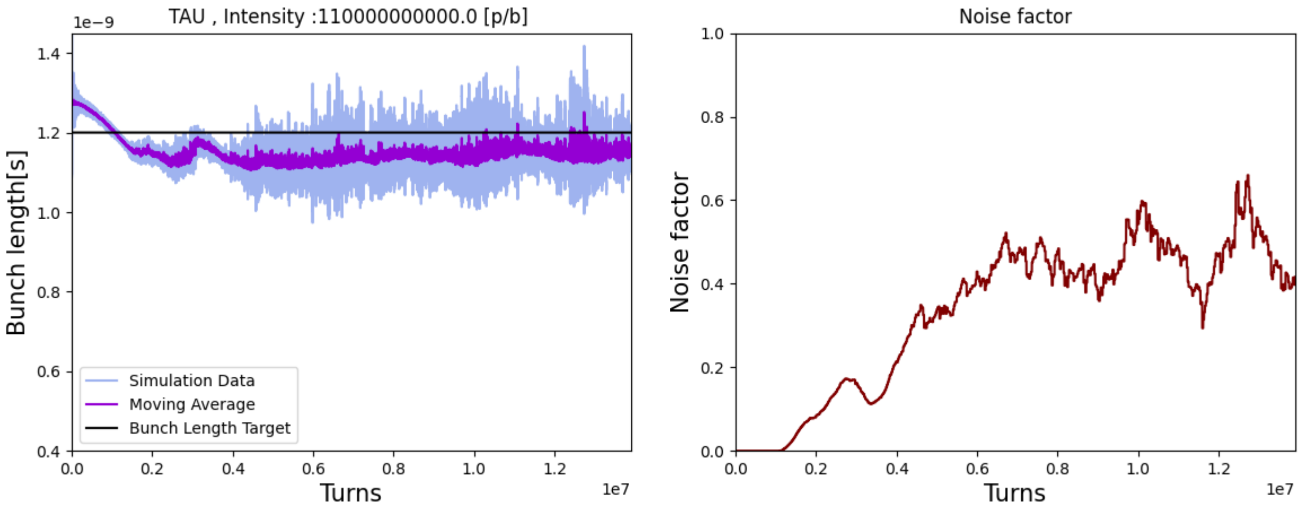

Figure 5.8: Bunch length evolution (left) during the LHC ramp with an initial bunch length of 1.65 nsec at LHC capture and an intensity of 1.1×10^{11} p/b. BLonD simulation data (blue), its smoothed value using a moving average (purple), and the target bunch length (black) are plotted as a function of time. Noise amplitude evolution (right) during the ramp, as regulated by the bunch length feedback.

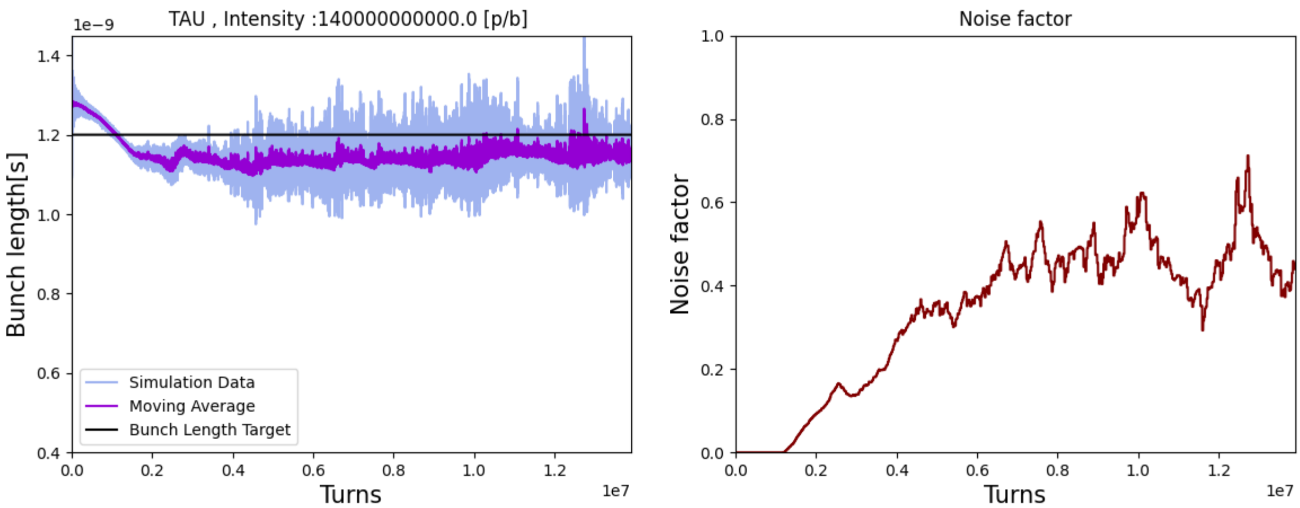

Figure 5.9: Bunch length evolution (left) during the LHC ramp with an initial bunch length of 1.65 nsec at LHC capture and an intensity of 1.4×10^{11} p/b. BLonD simulation data (blue), its smoothed value using a moving average (purple), and the target bunch length (black) are plotted as a function of time. Noise amplitude evolution (right) during the ramp, as regulated by the bunch length feedback.

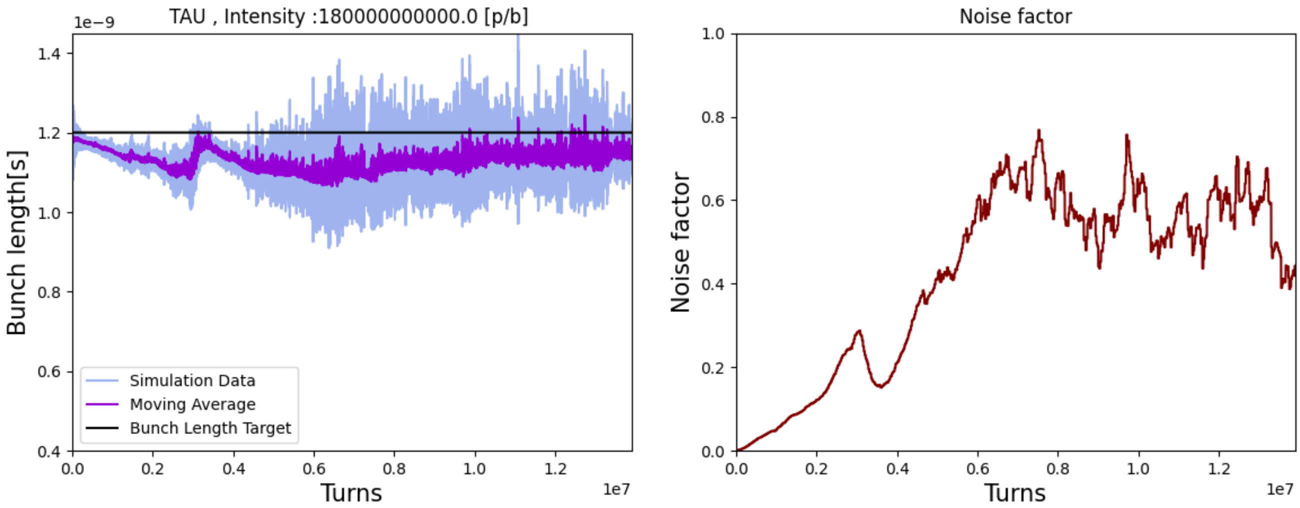

Figure 5.10: Bunch length evolution (left) during the LHC ramp with an initial bunch length of 1.65 nsec at LHC capture and an intensity of 1.8×10^{11} p/b. BLonD simulation data (blue), its smoothed value using a moving average (purple), and the target bunch length (black) are plotted as a function of time. Noise amplitude evolution (right) during the ramp, as regulated by the bunch length feedback.

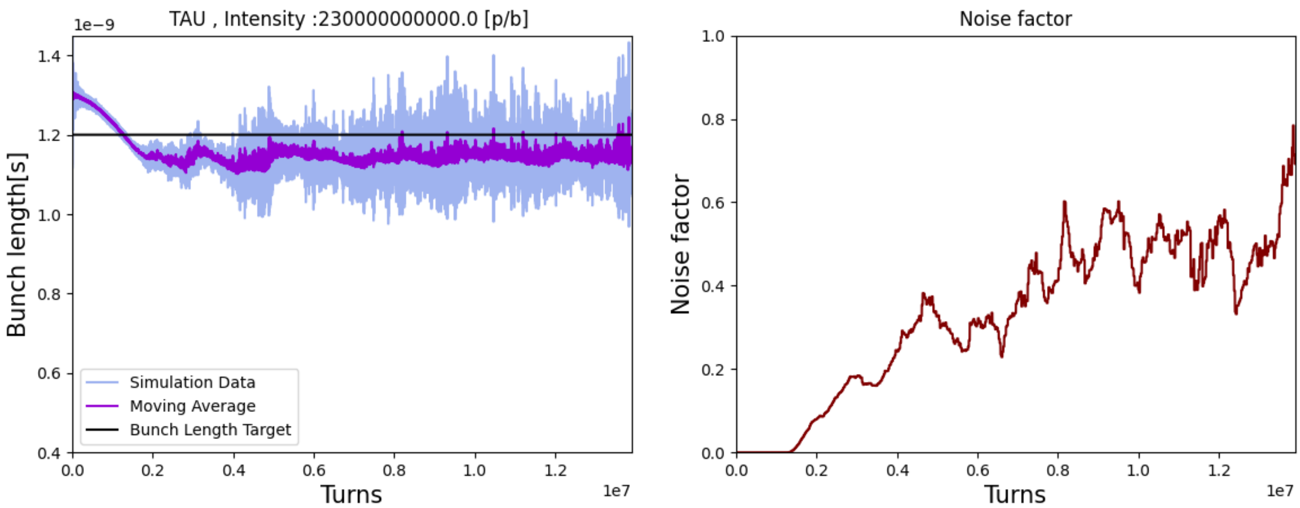

Figure 5.11: Bunch length evolution (left) during the LHC ramp with an initial bunch length of 1.65 nsec at LHC capture and an intensity of 2.3×10^{11} p/b. BLonD simulation data (blue), its smoothed value using a moving average (purple), and the target bunch length (black) are plotted as a function of time. Noise amplitude evolution (right) during the ramp, as regulated by the bunch length feedback.

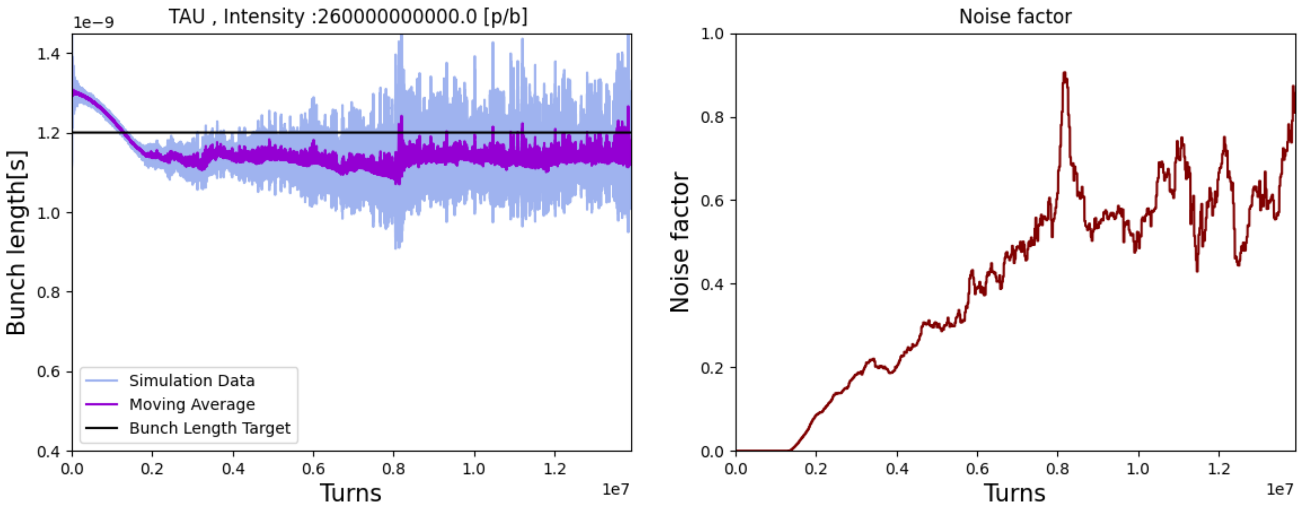

Figure 5.12: Bunch length evolution (left) during the LHC ramp with an initial bunch length of 1.65 nsec at LHC capture and an intensity of 2.6×10^{11} p/b. BLonD simulation data (blue), its smoothed value using a moving average (purple), and the target bunch length (black) are plotted as a function of time. Noise amplitude evolution (right) during the ramp, as regulated by the bunch length feedback.

6 Conclusions and outlook

In conclusion, this thesis studies controlled longitudinal emittance blow-up for single bunches in the LHC Run 3 and HL-LHC eras using the BLonD simulation suite.

The stability of single bunches has been studied throughout the LHC acceleration ramp, in the absence of beam control loops and RF noise. To determine the threshold of instabilities, we applied a suitable chosen threshold on the bunch length oscillations. This resulted in a consistent description of stable and unstable cases for the studied parameter range. Comparing to the threshold of loss of Landau damping, it was also concluded that the instabilities occur much later in the ramp.

The operational method for controlled emittance blow-up is modelled using the same noise generation and bunch length feedback algorithms as well as noise spectrum as is presently implemented in the machine. The simulations make use of accurate models of the exisiting LHC beam phase and synchronization loops. The blow-up has also been studied for the LHC Run 3 and HL-LHC eras, using the expected SPS bunch emittance at extraction and operational voltages in the LHC. In all cases, the presently used operational method for the blow-up regulated the bunch length well throughout the entire ramp. The bunch profile at arrival to flat top is round with little shoulders and virtually no losses occurred during the ramp.

The simulation studies of controlled noise injection during the ramp will be continued in the future. On one hand, the LHC impedance model has to be refined and this might affect the simulation results. On the other hand, the question remains whether for multi-bunch cases the operational blow-up will be able to properly regulate the bunch length at HL-LHC intensities. At the moment, these simulations are computationally too expensive and a GPU-accelerated version of BLonD is underway to make such simulations possible.

The simulation tools that were set up for this thesis to study this complicated manipulation include collective effects, control loops, and controlled noise injection. These tools remain available and are a valuable starting point for future studies with many bunches.

A Detected instability thresholds

Below, we present the plots of bunch length oscillations that are used in Chapter 4 to detect the threshold of single-bunch instabilities throughout the ramp.

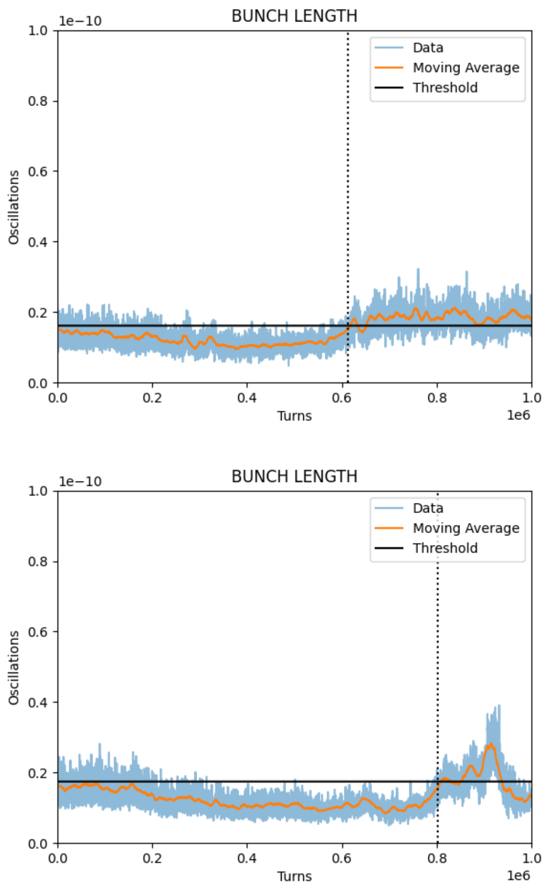

Figure A.1: Bunch length oscillations for and intensity of 1.4×10^{11} p/b and with and initial bunch length of 1.1 ns (top) and 1.2 ns (bottom).

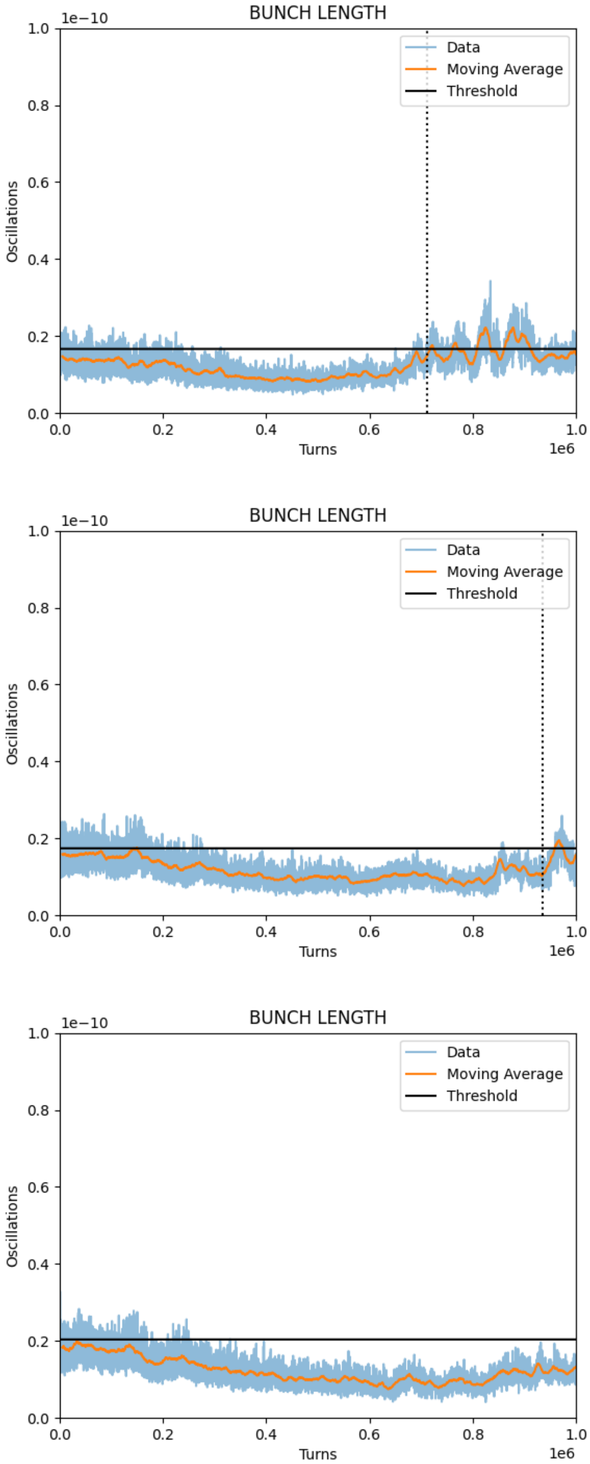

Figure A.2: Bunch length oscillations for and intensity of 1.1×10^{11} p/b and with and initial bunch length of 1.1 ns (top), 1.2 ns (middle), and 1.3 ns (bottom).

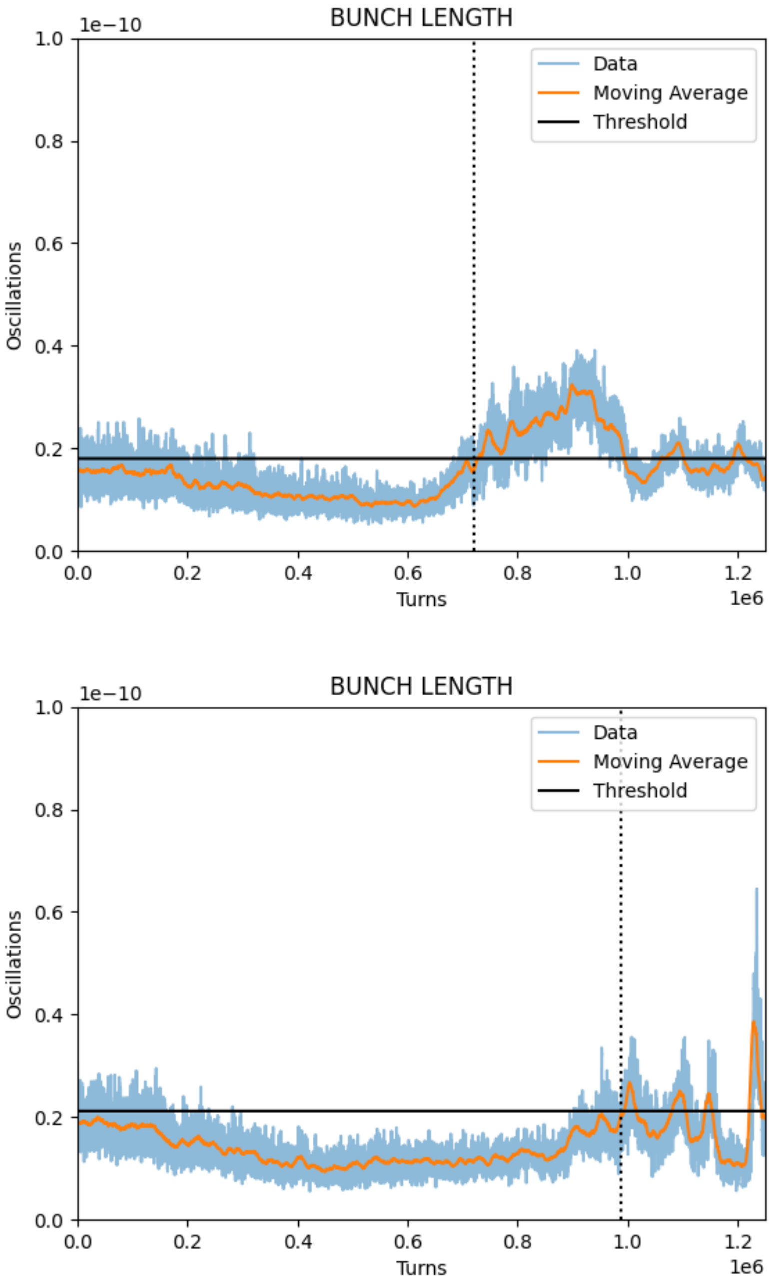

Figure A.3: Bunch length oscillations for and intensity of 1.8×10^{11} p/b and with and initial bunch length of 1.2 ns (top) and 1.3 ns (bottom).

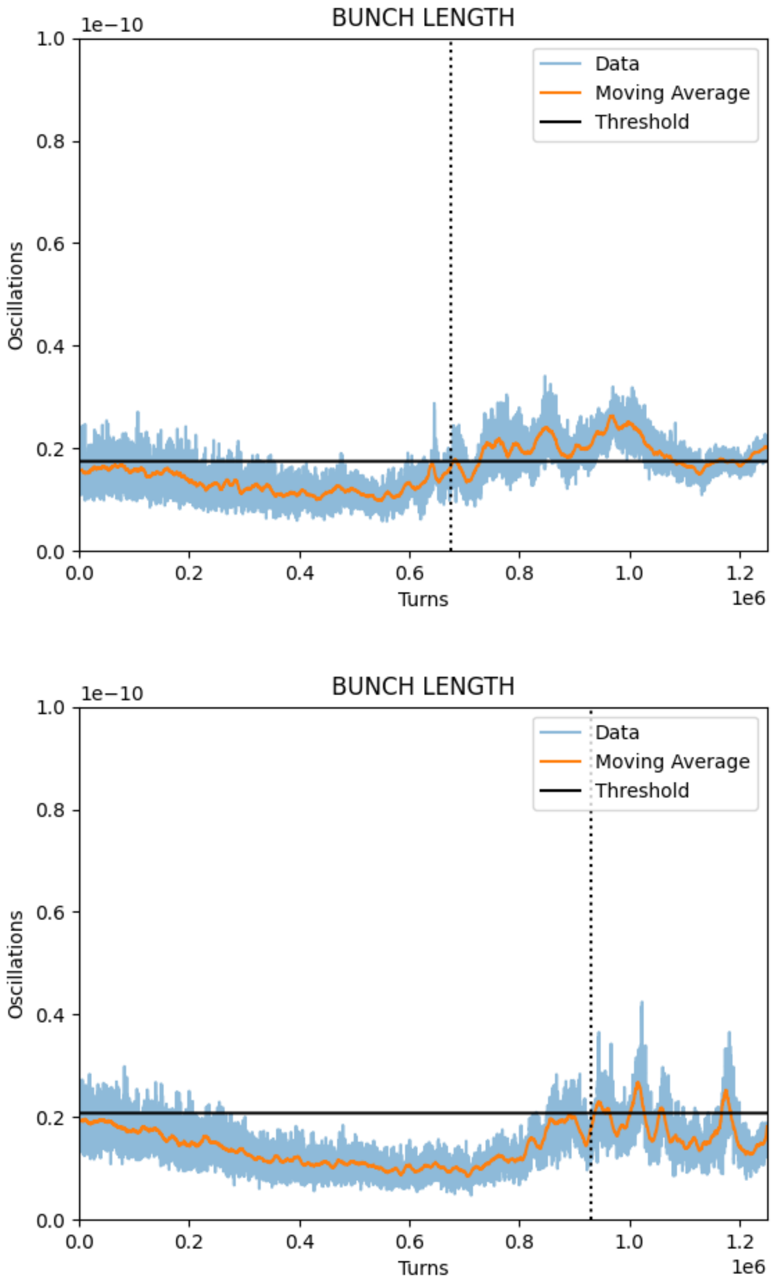

Figure A.4: Bunch length oscillations for and intensity of 2.1×10^{11} p/b and with and initial bunch length of 1.2 ns (top) and 1.3 ns (bottom).

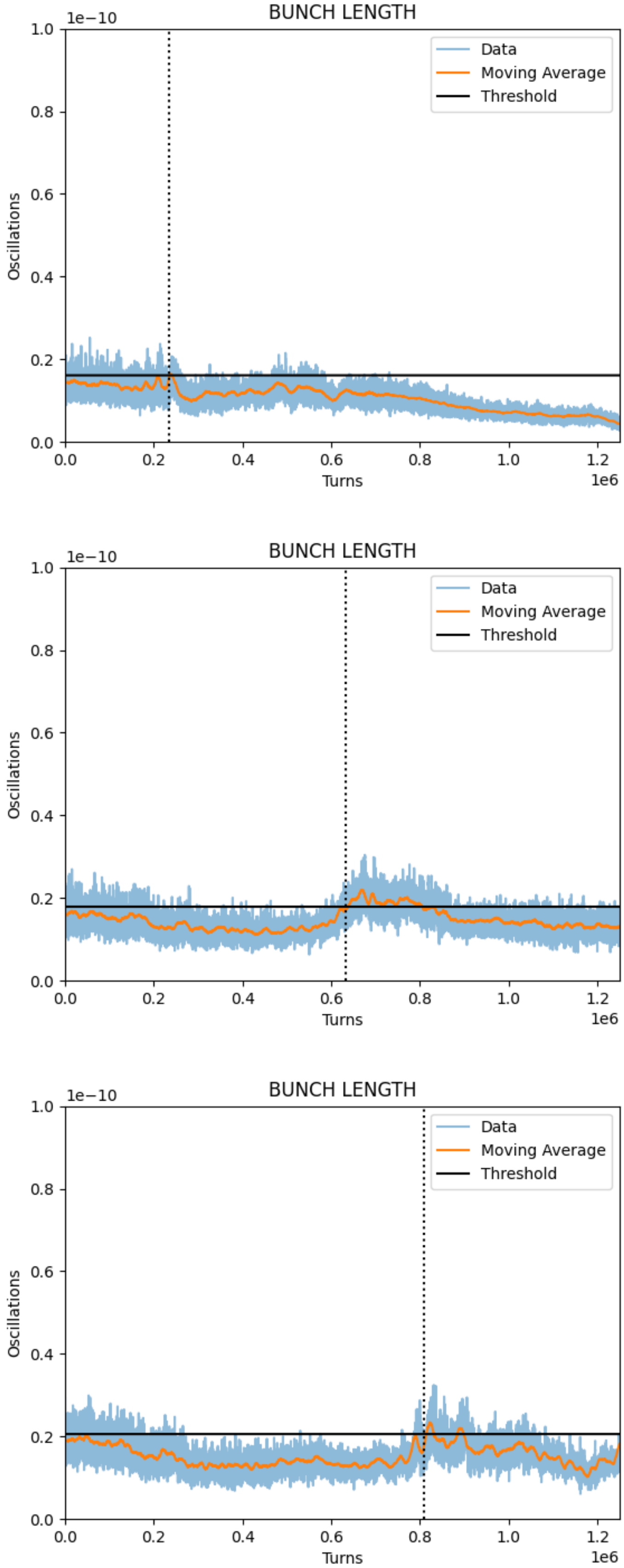

Figure A.5: Bunch length oscillations for and intensity of 2.3×10^{11} p/b and with and initial bunch length of 1.1 ns (top), 1.2 ns (middle), and 1.3 ns (bottom).

Bibliography

[1] *CERN's accelerator complex.* URL: https://home.cern/science/accelerators/accelerator-complex.

[2] *The Large Hadron Collider.* URL: https://home.cern/science/accelerators/large-hadron-collider.

[3] O S Brüning et al. *LHC Design Report.* CERN Yellow Reports: Monographs. Geneva: CERN, 2004. DOI: 10.5170/CERN-2004-003-V-1. URL: https://cds.cern.ch/record/782076.

[4] H Timko et al. "Coping with longitudinal instabilities using controlled emittance blow-up". In: (2020), 6 p. DOI: 10.23732/CYRCP-2020-009.84. URL: https://cds.cern.ch/record/2751717.

[5] S.Y. Lee. *Accelerator physics.* 2004.

[6] Baird S. "Taking a closer look at LHC". In: (2007).

[7] H. Timko. *BLonD equations of motion.*

[8] B. Muratori W. Herr. *Concept of luminosity.* CERN, Geneva, Switzerland.

[9] O. Aberle et al. *High-Luminosity Large Hadron Collider (HL-LHC): Technical design report.* CERN Yellow Reports: Monographs. Geneva: CERN, 2020. DOI: 10.23731/CYRM-2020-0010. URL: https://cds.cern.ch/record/2749422.

[10] H Damerau et al. *LHC Injectors Upgrade, Technical Design Report.* Dec. 2014. DOI: 10.17181/CERN.7NHR.6HGC. URL: https://cds.cern.ch/record/1976692.

[11] H. Timko. *RF Parameters throughout Run III.* Talk at the 10th LHC Run-III Configuration Meeting. 2019. URL: https://indico.cern.ch/event/796630/#6-rf-settings-in-run-iii.

[12] H. Timko et al. *LHC RF: Possible Limitations and Planned Run 3 Studies.* Talk at the LHC Performance Workshop 2022. 2022. URL: https://indico.cern.ch/event/1097716/contributions/4618900/.

[13] G. Arduini B. Salvant O. Aberle. "LHC impedance model: experience with high intensity operation in the LHC". In: (2012).

[14] B Salvant et al. "LHC Impedance Model: Experience with High Intensity Operation in the LHC". In: Sept. 2012.

[15] W. Herr. *Introduction to Landau Damping.* CERN, Geneva, Switzerland, 2014.

[16] A Hofmann. "Landau damping; 2006 ed." In: (2006). DOI: 10.5170/CERN-2006-002.271. URL: https://cds.cern.ch/record/941315.

[17] I. Karpov E. Shaposhnikova T. Argyropoulos. "Landau damping in the longitudinal plane". In: (2020), 6 p. DOI: 10.23732/CYRCP-2020-009.54. URL: https://cds.cern.ch/record/2751714.

[18] E. Shaposhnikova I. Karpov T. Argyropoulos. "Thresholds for loss of Landau damping in longitudinal plane". In: *Phys. Rev. Accel. Beams* 24 (Nov. 2020). 40 pages, 18 figures, 011002. 19 p. DOI: 10.1103/PhysRevAccelBeams.24.011002. arXiv: 2011.07985. URL: https://cds.cern.ch/record/2748559.

[19] P. Baudrenghien et al. "The LHC Low Level RF". In: (July 2006). revised version submitted on 2006-08-28 14:51:11, 4 p. URL: https://cds.cern.ch/record/971742.

[20] P. Baudrenghien. "Low-level RF - Part I: Longitudinal dynamics and beam-based loops in synchrotrons". In: (2012). DOI: 10.48550/ARXIV.1201.2597. URL: https://arxiv.org/abs/1201.2597.

[21] K. Iliakis. "Large-scale software optimization and micro-architectural specialization for accelerated high-performance computing". PhD thesis. National Technical University of Athens, 2022.

[22] H. Timko et al. "Studies on Controlled RF Noise for the LHC". In: *Proc. HB2014*. THO4LR03. East Lansing, U.S.A., 2015. URL: https://cds.cern.ch/record/2159006.

[23] S V Ivanov. *Longitudinal diffusion of a proton bunch under external noise*. Tech. rep. IHEP-92-43. Protvino, Russia: Protvino Inst. High Energy Phys., Mar. 1992. URL: https://cds.cern.ch/record/241368.

[24] P Baudrenghien and T Mastoridis. "Longitudinal emittance blowup in the large hadron collider". In: *Nucl. Instrum. Methods Phys. Res., A* 726 (2013), pp. 181–190. DOI: 10.1016/j.nima.2013.05.060. URL: https://cds.cern.ch/record/1709247.

[25] J. Tückmantel. *Digital Generation of Noise-Signals with Arbitrary Constant or Time-Varying Spectra (A noise generation software package and its application)*. Tech. rep. LHC-PROJECT-Report-1055. Geneva: CERN, 2008. URL: https://cds.cern.ch/record/1088050.